Open Archive Toulouse Archive Ouverte (OATAO)

To cite this version :

Robust Active Mirror Control Based on Hybrid Sensing for Spacecraft Line-of-Sight Stabilization

Francesco Sanfedino, Valentin Preda, Valérie Pommier-Budinger, Daniel Alazard, Fabrice Boquet, and Samir Bennani

Abstract—Modern space observation missions demand stringent pointing requirements that motivated a significant amount of research on the topic of microvibration isolation and line-of-sight stabilization systems. While disturbances can be reduced by mounting some of the noisy equipment on various isolation platforms, residual vibrations can still propagate through and be amplified by the flexible structure of the spacecraft. In order to alleviate these issues, the line-of-sight must also be actively controlled at the payload level. However, such systems typically have to rely solely on low frequency sensors based on image processing algorithms. The goal of this paper is to present a model-based control methodology that can increase the bandwidth of such systems by making use of additional rate sensors mounted on the main disturbance elements impacting the optical path. Following a comprehensive model identification and uncertainty quantification part, the robust control strategy is designed to account for plant uncertainty and provide formal worst-case performance guarantees. Excellent agreement between theoretical prediction and experimental results are obtained on a test bench developed at the European Space Agency.

Index Terms—Fast steering mirror, hybrid sensing, microvibrations, pointing stability, robust control.

I. Introduction

THE main concern of modern high accuracy Space missions is the isolation of on-board microvibrations, that can severely impact the performances of sensitive optical equipment. These low amplitude vibrations are mostly generated by mechanical devices such as reaction wheels (RW), control moment gyroscopes (CMG), cryocoolers or solar array drive mechanisms (SADM) [1] and can span a large bandwidth ranging from a few Hz to several hundreds Hz. In addition, due to the flexible nature of the spacecraft, these microvibrations can be significantly amplified around the resonant frequencies of the structure and strongly limit the achievable optical performance.

Earth observation Space missions and astronomical telescopes thus suffer from permanent degradation on the information gathered in the recorded images. However, in many instances, noisy equipment is critical to ensure the correct orientation, temperature control or power supply of the entire spacecraft and cannot be simply turned off during the imagining window. Therefore, there is a significant need to develop microvibration management systems that ensure high levels of line-of-sight stability. For example, NASA's *Hubble Space Telescope* (HST) is one of the first bench studies for a high-accuracy pointing system with a performance requirement of 0.01 arcsec [2]. Modern missions, such as the *James Webb Space Telescope* (JWST) [3] and *Euclid* [4] even aim nano-radian precision for their optical payload.

To achieve these demanding goals, a relevant research effort focused on developing better mathematical models of the main microvibration sources, namely RWs and CMGs, used for attitude control [5]–[11]. These generate speed-dependent harmonic perturbations due to mass imbalances in the rotating flywheel, ball bearing or motor imperfections. A significant number of passive and active isolation strategies have been proposed that specifically target the vibrations induced by such equipment. For example, the flywheels of the HST were isolated by introducing a supplementary damping element between the disturbing forces/torques and the spacecraft hub to reduce the transmissibility function [2]. Unfortunately, the main drawback of passive isolators is that they only attenuate high frequency noise and can even degrade the performance in the low frequency by introducing new flexible modes with a low damping ratio. Furthermore, for a solution based solely on passive isolators, there exists a fundamental trade-off between high frequency attenuation and peak gain at the natural frequency. A widely adopted idea to overcome such limitations is to combine passive isolator with active control into so-called hybrid passive/active isolation systems. For example [12], [13] proposed and tested a low frequency flexible platform comprised of four folded continuous beams arranged in three dimensions. In [14] magnetorheological elastomers were used to build smart sandwich beams for microvibration isolation. Another common configuration is the so-called Stewart or hexapod platform [15]–[17] where six active (or hybrid) legs are used to actuate and stabilize the platform supporting the disturbance source. This arrangement was also used by [18] on the Micro-Precision Interferometer test bed in order to demonstrate six degrees of freedom vibration

isolation. In [19] an original hybrid isolators configuration was proposed consisting of an active plate mounted on top of passive elastomer isolators. The forces and torques transmitted to the base structure are measured using a group of piezo-electric force cells and control inputs are computed for a set of six proof-mass actuators mounted on the active plate. The setup was further developed in [9]–[11] by adopting an innovative $\mathcal{H}_\infty$/LPV robust control strategy that schedules the controller based on the flywheel speed.

However, isolation at the disturbance source level for some electromechanical subsystems such as SADM or antenna trimming motors can be challenging from the point of view of mechanical complexity. To compensate for the residual LOS errors, the degraded optical path can also be also corrected at the payload level by means of various active optics systems. For example, Neat *et al.* [18] combined piezo-electric fast steering mirror and voice coils for spaceborn optical interferometers to meet sub-micron accuracy. Somov *et al.* [20] proposed a fine image motion stabilization for flexible large-scale remote sensing spacecraft. Canuto [21] presented an observer-based control strategy for piezo-electric actuators employed in the global astrometric interferometer for astrophysics (GAIA) mission. The JWST [22] mounts a fine pointing device driven at 30 Hz by voice coils. Sun *et al.* [23] designed and validated experimentally a payload-platform driven by four piezo-electric actuators coupled with displacement amplifier to isolate microvibrations up to 5 Hz. However, in these systems the full potentiality of the actuators is underexploited because of the limitations imposed by the sensing devices.

In this context, the main focus and contribution of this paper is to propose a hardware-in-the-loop facility to assess internal disturbance rejection using the full capability of the piezo-electric technology in order to drive an FSM to mitigate the microvibrations up to 100 Hz. The target mission is a Space telescope the optical payload of which has a low bandwidth and a considerable integration time, like a CCD camera. The novelty of the approach is the introduction of a fast Angular Rate Sensor (ARS-14 by Applied Technology Associates [24]) based on the magneto-hydrodynamic (MHD) effect. This compact sensor is Space qualified and can be installed on the most sensitive optical element in the telescope, generally the primary mirror, to collect the LOS distortions transmitted by all the vibration sources. A robust control synthesis is proposed to fusion the measurements provided by the CCD camera and the ARS-14 in a $\mu/\mathcal{H}_\infty$ framework [25]–[29] directly in the frequency domain. This framework was selected among the different linear controller design techniques in order to find an optimal balance between the various constraints and objectives expressed in the frequency domain [29]. Other techniques such as nonlinear control were not investigated due to the linear behavior of the considered plant.

Thanks to multi-sensor fusion, that benefits from the CCD outputs at low frequency and from the ARS outputs in the high frequency (usable bandwidth between 2 and 2000 Hz), it is possible to extend the control bandwidth up to 100 Hz. An experimental test bench developed at the European Space Agency (ESA-ESTEC) laboratories serves as validation of this approach. This setup is used for a double objective:

1) to set up a high-fidelity benchmark to replicate the LOS jitter of a Space mission with a hardware-in-the-loop configuration. This task is carried out by a Disturbing Fast Steering Mirror (DFSM) equipped with an MHD sensor. The objective of the DFSM is to generate a calibrated disturbance based on a model of the microvibrations and deflect a laser beam. This model can be adapted according to any specific observation Space mission. An example of such a model is detailed in Section III-C;

2) to validate a novel microvibration control architecture based on multi-sensor fusion and a Control Fast Steering Mirror (CFSM) to improve the traditional pointing performances by extending the rejection bandwidth to 100 Hz and reduce the transmitted disturbances at least by 10 dB. Formal proof of stability and performance guarantees is provided as well in the *structured singular value* framework in order to make this system robust to any model uncertainty.

The methodology presented in this paper is based on the assumption that the system is subjected to small deflections and the hypothesis of linear dynamics holds. This assumption includes the majority of Space applications, that generally avoid large deflections and nonlinear behaviour of the structures by design. In cases where this hypothesis has to be removed, the specific nonlinearity is taken into account in control tuning and validation phases. The common practice consists then in iterating between a linear controller design and a Monte-Carlo analysis of the full nonlinear plant model.

The experimental setup is first presented in Section II-A. The method used for identification is then described in Section II-B. The control architecture used for the DFSM tracking problem and for the LOS stabilization with the CFSM are respectively outlined in Section II-C and Section II-D. Section III shows the experimental results with analysis of the stability and performance robustness of the system. A short application of the setup for spacecraft scenario simulation is finally presented in Section III-C.

II. Materials and Methods

A. Experimental setup

The experimental bench used in this study, shown in Fig. 1c, aims to represent a simplified Space telescope observation mission. By taking as reference a Korsch telescope [30] (see Fig. 1), displacements in the primary mirror relative to the imaging sensor are assumed to be the biggest contributor to the overall LOS error. The disturbance in the LOS due to the relative movement of other optical elements is considered negligible in comparison.

Furthermore, the rigid body of the satellite is assumed to be in perfect alignment with the target object.

In accordance with the previously described mission, the setup is composed of two piezo-electric Fast Steering Mirrors (FSMs), an autocollimator and an angular rate sensor attached to one of the active mirrors. The autocollimator (CONEX-LDS by Newport [31]) sends a laser beam that reflects off the two mirrors and then returns back on a position sensor embedded within the device. Based on these sensor measurements, the angle between the outgoing and incoming rays is calculated down to sub micro rad resolution with a maximum acquisition frequency of 2000 Hz. In this study, the autocollimator is used to simulate a low-bandwidth LOS error measurement system based upon a camera and an image processing algorithm. Therefore, the acquisition frequency of the autocollimator is reduced and high frequency noise is added to match that of a typical imaging sensor. Furthermore a variable time delay is added to simulate the image processing time. This new sensor block will be subsequently called virtual CCD or simply CCD. The DFSM, product manufactured by CEDRAT Technologies, is used to simulate the typical pointing errors induced by the microvibration sources by deflecting the autocollimator laser beam. As shown in Fig. 1c, a single-axis ARS is mounted on the DFSM in order to measure the deflection rate of the mirror around the axis parallel to the table.

The schematic diagram of the microvibrations control is shown in Fig. 2. The software part is implemented in the MicroLabBox provided by dSpace.

Two independent controllers are needed. The DFSM controller takes as reference the LOS disturbing profile $\mathbf{r}$ and tracks it by using the strain gauge measurements $\mathbf{y}_{S_n}$ collocated with the piezoelectric actuators. The objective of this controller is to perfectly reproduce the demanded reference LOS error for a frequency up to 100 Hz and minimize any gain and phase distortions.

On the other hand the CFSM controller uses the measurements $\mathbf{y}_{C_n}$ and $\mathbf{y}_{A_n}$ obtained from the virtual CCD block and the angular rate sensor to provide the command $\mathbf{u}$. This command is used to drive the piezo-electric stack within the CFSM (model S-330.2SL produced by Physik Instrumente [32]) and stabilize the LOS. The challenge introduced by this architecture is the use of the ARS in feed-forward control: it directly measures the disturbances but is not affected by the CFSM control command $\mathbf{u}$. No high-rate measurements are thus available in feedback to know how well the CFSM is stabilizing the LOS. The performances of a feed-forward controller are known to be directly linked to the accuracy of the plant modeling. This is why a robust control synthesis in $\mu/\mathcal{H}_\infty$ framework was adopted to cover a large set of possible plant uncertainties and guarantee a certain level of robust closed-loop performance. Note that this paper focuses on LOS stabilization along a single axis for simplicity's sake. However, the techniques presented in this work can be extended to the dual-axis LOS control problem without significant changes to the overall methodology.
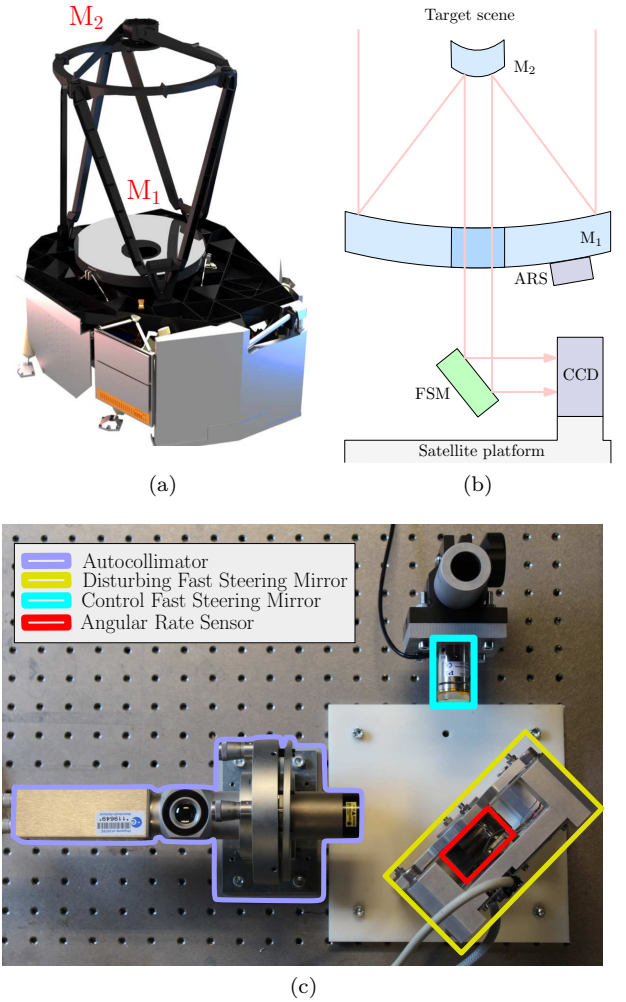

Fig. 1. (a) Mirror architecture for the Euclid mission. Image credit: Airbus Defence and Space. (b) Schematic of the space application considered in this study (c) ESA's experimental setup for line-of-sight stabilization.

B. Model identification method

The goal of plant identification is to find mathematical models that describe the two uncertain systems to be controlled: the DFSM $\bar{\mathbf{G}}_D$ for reference LOS error tracking and the CFSM $\bar{\mathbf{G}}_{\text{LOS}}$ used for LOS stabilization. Their Linear Fractional Transformation (LFT) models are schematically represented in Fig. 3, with $\bar{\mathbf{G}}_D = \mathcal{F}_u(\mathbf{G}_D, \Delta_D)$ and $\bar{\mathbf{G}}_{\text{LOS}} = \mathcal{F}_u(\mathbf{G}_{\text{LOS}}, \Delta_{\text{LOS}})$, where $\mathcal{F}_u$ denotes the upper LFT. The basic idea of the LFT formalism is to express the process model as a feedback connection between the nominal plant and the uncertainty description of the system [27], [33].

The steps of the identification process are the following:

1) Recording of the sensor outputs without excitation of the outputs for noise characterization (strain gauge noise $\mathbf{n}_S$, autocollimator noise $\mathbf{n}_L$ and ARS noise $\mathbf{n}_A$). The background noise caused by external sources such as air-conditioning, road traffic together with the electrical noise from the main supply (50 Hz and harmonics) is integrated in these measurements. The hypothesis taken here is that the environment influ-
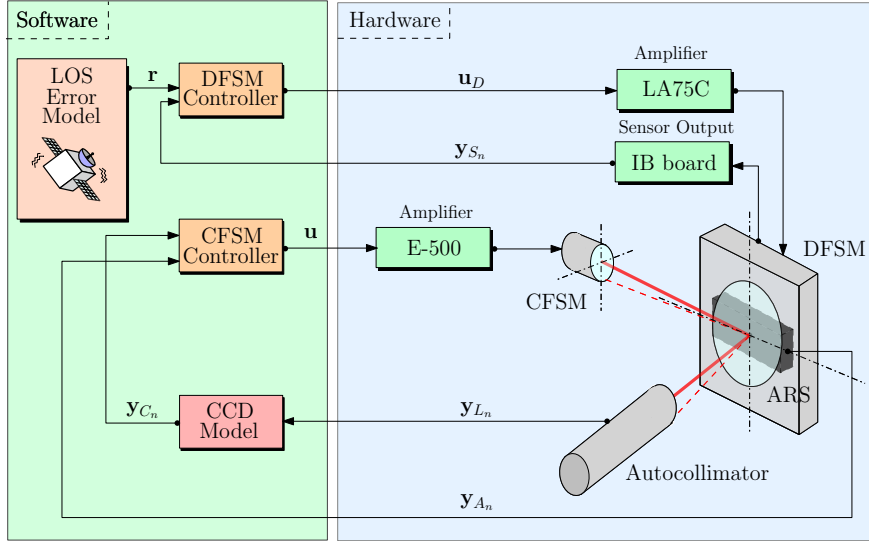
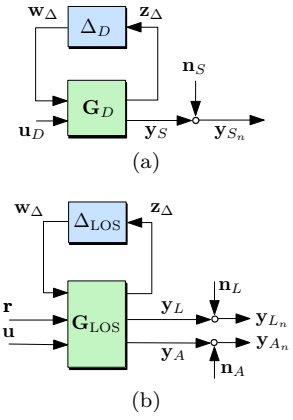Fig. 2. Hardware-in-the-loop facility architecture.

Fig. 3. LFT models and output noise signals of the two plants: (a) Disturbance Fast Steering Mirror, (b) LOS stabilization with combined Control Fast Steering Mirror, autocollimator and ARS sensor blocks.

ences directly the output measurements and not the inputs of the system. This hypothesis is due to the difficulty to exactly separate the contribution of the noise due to sensing and/or the external disturbances.

2) Excitation, in turn, of each input by a logarithmic chirp with maximum amplitude set at 90% of the maximum feasible value and record of the sensor outputs.

3) Estimation of the Amplitude Spectrum (AS) of the noises.

4) Non-parametric estimation of the nominal plants and the variance of the system spectral estimate by Spectral Analysis method [34]. According to this method the Frequency Response Function (FRF) of the plant $G(s)$, with s Laplace variable, is computed as the ratio between the cross spectrum $\Phi_{yu}(s)$ and the autopower spectrum $\Phi_{uu}(s)$ of the input-output signals [35]:

$$G(s) = \frac{\Phi_{yu}(s)}{\Phi_{uu}(s)}. \tag{1}$$

The Welch method [36] gives an estimation of $\Phi_{yu}(s)$ and $\Phi_{uu}(s)$ by splitting the N input-output samples in M subrecords of N/M samples each. If $\left(X(k)^{[m]}\right)_W$ is the windowed Discrete Fourier Transform (DFT) of the signal $x(t)$ computed on N/M samples and defined by

$$\left(X(k)^{[m]}\right)_W = \frac{1}{w_{\mathrm{rms}}\sqrt{\beta}} \sum_{n=0}^{\beta-1} w(nT_s)x(nT_s)e^{-j\frac{2\pi kn}{\beta}}, \tag{2}$$

with $\beta = N/M$, T_s sampling period and $w_{\mathrm{rms}} = \left(\sum_{n=0}^{N/M-1} |w(nT_s)|^2/(N/M)\right)^{1/2}$ the root mean square of the window $w(t)$, the estimate of the cross- and autopower spectra is respectively given by

$$\hat{\Phi}_{Y_W U_W}(k) = \frac{1}{M} \sum_{m=1}^{M} \left(Y^{[m]}(k)\right)_W \overline{\left(U^{[m]}(k)\right)_W}, \tag{3}$$

with $\overline{U}$ complex conjugate of U and

$$\hat{\Phi}_{U_W U_W}(k) = \frac{1}{M} \sum_{m=1}^{M} \left|\left(U^{[m]}(k)\right)_W\right|^2. \tag{4}$$

Using (3) and (4) the estimate of the plant in (1) is thus given by

$$\hat{G}(k) = \frac{\hat{\Phi}_{Y_W U_W}(k)}{\hat{\Phi}_{U_W U_W}(k)}. \tag{5}$$

The quality of the spectral estimate (5) is quantified by the coherence spectrum $\Gamma(k)$

$$\Gamma(k) = \frac{\left|\hat{\Phi}_{Y_W U_W}(k)\right|^2}{\hat{\Phi}_{Y_W Y_W}(k)\hat{\Phi}_{U_W U_W}(k)}, \tag{6}$$

which is a value between 0 and 1 that highlights the presence of a disturbing noise, nonlinear distortions, residual leakage errors or a non-observed input [35] when it is smaller then unity. The variance of the spectral analysis estimate is thus defined as

$$\hat{\sigma}^2(k) = \frac{1 - \Gamma(k)^2}{\Gamma(k)^{1/2}} \left|\hat{G}(k)\right|^2. \tag{7}$$

5) Fitting the amplitude spectrum obtained at step 3 with continuous-time minimum-phase state-space model using log-Chebyshev magnitude design [37], [38] with the MATLAB function *fitmagfrd*.

6) Continuous-time transfer function estimation of the nominal plants $G(s)$ using the discrete-time frequency-domain data obtained at step 4 in (5) with fixed number of poles and zeros [39], [40] and by enforcing stability, with the MATLAB function *tfest* of the System Identification Toolbox [34].

7) Fitting the frequency response magnitude data of the estimated total uncertainty model represented by the filter $\hat{W}_\Delta(k)$ with continuous-time minimum-phase

state-space model $W_\Delta(s)$ using log-Chebyshev magnitude design so that the total uncertainty on the plant results

$$\Delta(s) = W_\Delta(s)\widetilde{\Delta}(s), \quad ||\widetilde{\Delta}(s)||_\infty \le 1. \qquad (8)$$

$\hat{W}_\Delta(k)$ is due to two contributions:

- **Spectral estimate uncertainty** $\hat{W}_{\Delta_{np}}(k)$ computed on one standard deviation of the system estimate:

$$\hat{W}_{\Delta_{np}}(k) = \sqrt{\hat{\sigma}^2(k)} \qquad (9)$$

- **Additive model fitting uncertainty** $\hat{W}_{\Delta_p}(k)$ due to the difference between the non-parametric estimation of the nominal plant $\hat{G}(k)$ (step 4) and the continuous transfer function $G(s)$ (step 5) sampled at T_s,

$$\hat{W}_{\Delta_p}(k) = G(k) - \hat{G}(k). \qquad (10)$$

The total estimated uncertainty $\hat{W}_\Delta(k)$ is finally represented by the filter

$$\hat{W}_\Delta(k) = \left| \hat{W}_{\Delta_{np}}(k) \right| + \left| \hat{W}_{\Delta_p}(k) \right| \qquad (11)$$

These uncertainties will be used in the next section to directly design the weighting filters.

C. Disturbing Fast Steering Mirror control architecture and specifications

The DFSM controller has to insure perfect tracking of a disturbing LOS profile on a large bandwidth up to 100 Hz. Thus the synthesis and verification of this controller is overriding and essential to the LOS stabilization bench. The available DFSM has a local controller using the strain gauge measurements to overcome the problems of hysteresis and creep typical of piezoelectric actuators. The performances of the device have been estimated by preliminary identification studies. A bandwidth of ≈ 33 Hz and a phase shift of $180°$ at 100 Hz have been measured. The complexity to drive and identify the DFSM in open-loop without inducing any damage in the mirror gave rise to the development of a new control to extend the bandwidth and rectify the phase.

The designed controller $\mathbf{K}_D$ is used to generate the control signal $\mathbf{u}_D(t)$ with $\mathbf{u}_D = \mathbf{K}_D \begin{bmatrix} \mathbf{r} & | & \mathbf{y}_{S_n} \end{bmatrix}^{\mathrm{T}}$, where $\mathbf{r}(t)$ is the reference profile to be tracked and $\mathbf{y}_{S_n}(t)$ represents the strain gauge sensor noise outputs. This controller has to meet stability and performance requirements:

(**R1**) **Robust stability**: Closed-loop stability must be guaranteed with respect to all considered uncertainties.

(**R2**) **Robust tracking performance and control effort performance**: The first performance goal is to replicate the reference signal up to 100 Hz without phase shift in the same bandwidth. The second goal is to not induce degradation of the actuator by keeping the control signals below manufacturer limits.

1) Closed loop transfer functions: The control synthesis in this work is defined in the $\mu/\mathcal{H}_\infty$ framework. The problem comes down to an optimization problem of the worst-case $\mathcal{H}_\infty$ norm among different closed-loop signals scaled by the so-called weighting functions.

Consider the control diagram in Fig. 4. The DFSM uncertain plant is represented by the block $\mathcal{F}_u(\mathbf{G}_D, \Delta_D)$. The diagonal transfer function $\mathbf{G}_{\text{ref}}$ represents the desired closed-loop transfer function between the sensor measurements $\mathbf{y}_S$ and the tip/tilt reference profiles $\mathbf{r}$. The weighting functions are labeled $\mathbf{W}_\bullet$ and they are classified in two categories: the input weights as $\mathbf{W}_r$ and $\mathbf{W}_{n_S}$, which are respectively used to scale the amplitude spectrum of the reference $\mathbf{r}$ and the sensor noise $\mathbf{n}_S$, and the performance weights $\mathbf{W}_{e_t}$ and $\mathbf{W}_{u_D}$, which are used to place the upper bounds respectively of the tracking error $\mathbf{e}_t$ and of the control effort $\mathbf{u}_D$.

According to Fig. 4, the general open-loop interconnection can be written in terms of the complex uncertainty channels $\mathbf{w}_\Delta$ and $\mathbf{z}_\Delta$, the disturbances $\mathbf{d}_D = \begin{bmatrix} \mathbf{d}_r & \mathbf{d}_{n_S} \end{bmatrix}^{\mathrm{T}}$ and the performance channels $\mathbf{e}_D = \begin{bmatrix} \mathbf{e}_{e_t} & \mathbf{e}_{u_D} \end{bmatrix}^{\mathrm{T}}$ as well as the command $\mathbf{u}_D$ and the reference signal $\mathbf{r}$ and the noise sensor measurements $\mathbf{y}_{n_S}$ as in (12).

If now $\mathbf{K}_D = \begin{bmatrix} \mathbf{K}_r & | & \mathbf{K}_S \end{bmatrix}^{\mathrm{T}}$ is used to close the loop such that $\mathbf{u}_D = \mathbf{K}_D \begin{bmatrix} \mathbf{r} & | & \mathbf{y}_{S_n} \end{bmatrix}^{\mathrm{T}}$, define $\mathbf{S}_{i_D} = [\mathbf{I} + \mathbf{K}_S \mathbf{G}_{y_S u_D}]^{-1}$ and $\mathbf{T}_{i_D} = \mathbf{I} - \mathbf{S}_{i_D}$ as the input sensitivity and the input complementary sensitivity functions. Similarly, $\mathbf{S}_{o_D} = [\mathbf{I} + \mathbf{G}_{y_S u_D} \mathbf{K}_S]^{-1}$ and $\mathbf{T}_{o_D} = \mathbf{I} - \mathbf{S}_{o_D}$ denote the output sensitivity and the output complementary sensitivity functions. The closed-loop interconnection matrix $\mathbf{M}_D = \left[\begin{array}{c|c} \mathbf{M}_{D_{11}} & \mathbf{M}_{D_{12}} \\ \hline \mathbf{M}_{D_{21}} & \mathbf{M}_{D_{22}} \end{array} \right] = \mathcal{F}_l(\mathbf{P}_D, \mathbf{K}_D)$, where $\mathcal{F}_l$ denotes the lower LFT and with $\mathbf{M}_{D_{kj}} = \mathbf{P}_{D_{kj}} + \mathbf{P}_{D_{k3}} \mathbf{S}_{i_D} \mathbf{K}_D \mathbf{P}_{D_{3j}}$, takes the form (13).

2) Weighting functions selection: The input reference weight $\mathbf{W}_r$ is scaled with the maximum expected amplitude spectrum input reference to be tracked. A 4th-order Butterworth low-pass filter with cut-off frequency at 160 Hz is used:

The input weight $\mathbf{W}_{n_S}$ used to scale the strain gauges noise is provided by the system identification as explained in Section II-B at step 5. As shown in Fig. 5a a constant value is chosen for $\mathbf{W}_{n_S} = 3.5379 \cdot 10^{-2}$ mV.

The output weights $\mathbf{W}_{e_t}$ and $\mathbf{W}_{u_D}$ translate the performance requirement (**R2**) at Section II-C and their inverse represents the desired worst-case upper bounds on the amplitude spectrum of the tracking error $\mathbf{e}_t$ and the control signal $\mathbf{u}_D$. The limit of the achievable performances is given by the nominal performance matrix $\mathbf{M}_{D_{22}}$. The nominal requirements are in fact met if the condition $||\mathbf{M}_{D_{22}}||_\infty < 1$ holds. Consider the transfer function $\mathbf{M}_{D_{\mathbf{d}_r \to \mathbf{e}_{e_t}}} = \mathbf{W}_{e_t} (\mathbf{G}_{\text{ref}} - \mathbf{G}_{y_S u_D} \mathbf{S}_{i_D} \mathbf{K}_r) \mathbf{W}_r$ from the normalized reference $\mathbf{d}_r$ to the tracking performance $\mathbf{e}_{e_t}$ and assume that $\mathbf{W}_{e_t}$ has a high gain in a particular frequency region. In order to satisfy the condition $||\mathbf{M}_{D_{22}}||_\infty < 1$, the controller also has to shape
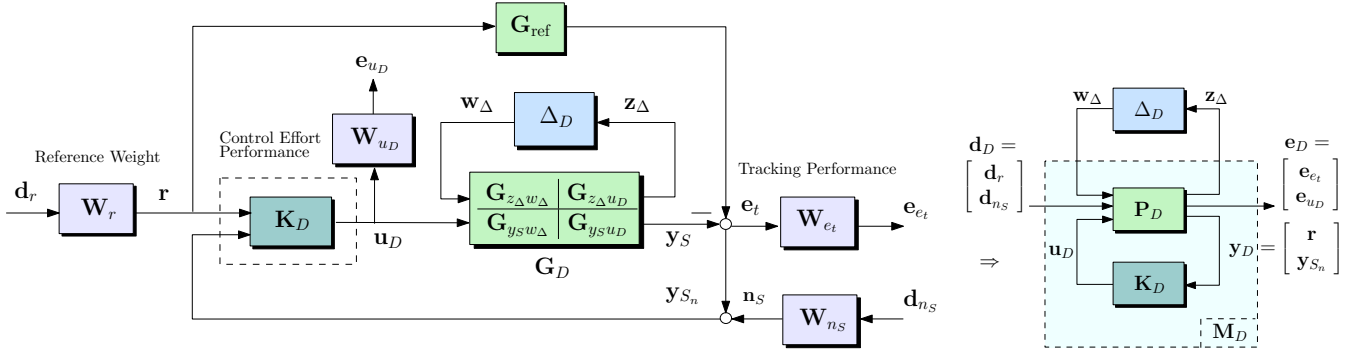
Fig. 4. Interconnection structure for synthesis and analysis of the Disturbing Fast Steering Mirror (DFSM).

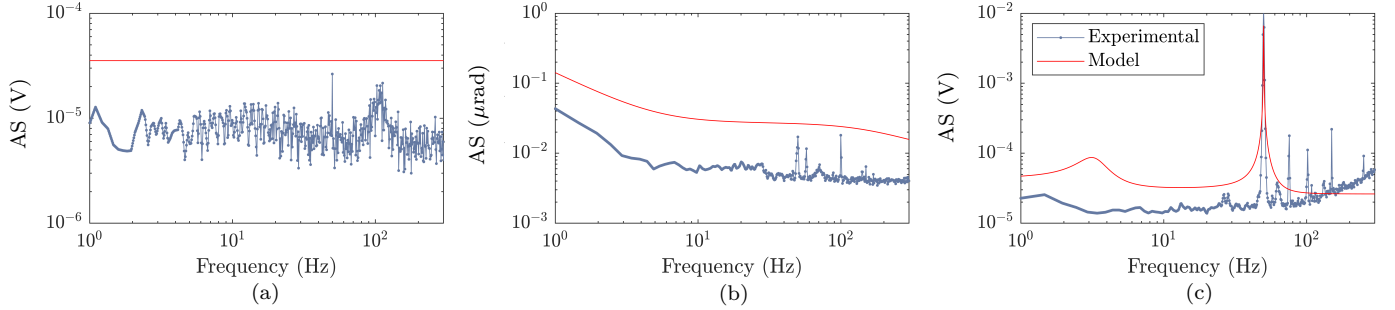Fig. 5. Amplitude Spectrum of the sensor noise: (a) DFSM strain gauges, (b) autocollimator, (c) ARS.

the function $\mathbf{S}_{i_D}\mathbf{K}_r$ with sufficiently high gain in the same frequency bandwidth and decrease the open-loop disturbance contribution to the tracking error $\mathbf{P}_{D_{\mathbf{d}_r \to \mathbf{e}_{e_t}}} = \mathbf{W}_{e_t}\mathbf{G}_{\mathrm{ref}}\mathbf{W}_r$.

According to these considerations the tracking weight $\mathbf{W}_{e_t}$ is chosen as a couple of parallel filters $\mathbf{W}_{e_t} = \left[\underline{\mathbf{W}}_{e_t} \ \overline{\mathbf{W}}_{e_t}\right]$. The weight $\underline{\mathbf{W}}_{e_t}$ is a 5th-order Butterworth low-pass filter with low-frequency gain $1/\underline{\varepsilon}_{\max}$, where $\underline{\varepsilon}_{\max} = 5\%$ is the upper bound on the tracking error, and cut-off frequency at $2\pi \cdot 150\,\mathrm{rad/s}$. On the other hand the weight $\overline{\mathbf{W}}_{e_t} = 1/\overline{\varepsilon}_{\max}$, with $\overline{\varepsilon}_{\max} = 10\%$ imposes an upper bound on the tracking error at high frequencies. The output weight $\mathbf{W}_{e_u}$ finally limits the control signal in the band of interest with the upper bound $\mathbf{W}_{u_D} = 0.04$.

D. LOS stabilization control architecture and specifications

Once the DFSM is able to replicate the desired LOS jitter, a controller is required to mitigate it on a large bandwidth up to 100 Hz. The CFSM controller is synthesized in the $\mu/\mathcal{H}_\infty$ framework by fusion of the measurements of the virtual CCD and the ARS.

The designed controller $\mathbf{K}$ is used to generate the control signal $\mathbf{u}(t)$ with $\mathbf{u} = \mathbf{K}\left[\begin{array}{cc} \mathbf{y}_{C_n} & \mathbf{y}_{A_n} \end{array}\right]^{\mathrm{T}}$, where $\mathbf{y}_{C_n}(t)$ represents the CCD outputs with noise and $\mathbf{y}_{A_n}(t)$ are the ARS measurements with noise. This controller has to meet stability and performance requirements:

(**R1**) **Robust stability**: Closed-loop stability must be guaranteed with respect to all considered uncertainties.

(**R2**) **Robust rejection and control effort performance**: The first performance goal is to reject all the disturbances to the LOS jitter caused by the DFSM deflection and the sensor measurements within 100 Hz to an upper bound of $10\,\mu\mathrm{rad}$. The second goal is to not induce degradation of the actuator by keeping the control signals below the manufacturer limits.

1) Closed loop transfer functions: Consider the interconnection structure for LOS stabilization in Fig. 6. The plant $\mathbf{G}_{\mathrm{LOS}}$ is shown in Fig. 1c, where the inputs are the reference signal $\mathbf{r}$ provided to the DFSM together with the control signal $\mathbf{u}$ and the outputs are the autocollimator and the ARS measurements, $\mathbf{y}_L$ and $\mathbf{y}_A$ respectively. Note that the transfer function $\mathbf{u} \to \mathbf{y}_A = \mathbf{0}$ because the control signal $\mathbf{u}$ does not affect the DFSM dynamic and the ARS measurements as a consequence.

The CCD camera model comprises three blocks: a second order low-pass Butterworth filter $\mathbf{G}_C$ with a cut-off frequency of 20 Hz, an uncertain fixed time delay $\tau = 10\,\mathrm{ms}$ modeled with a second order Pade approximation $\mathbf{G}_\tau$ with an additive uncertainty Δ_τ which takes into account the amplitude mismatch between the Pade approximation and a true time delay, a variable time delay τ_v modeled as a multiplicative uncertainty Δ_{τ_v}. The weighting filters $\mathbf{W}_{\Delta_\tau}$ and $\mathbf{W}_{\Delta_{\tau_v}}$ respectively scale the complex uncertainty $\Delta_\tau(s)$ s.t. $||\Delta_\tau(s)||_\infty \leq 1$ that takes into account the mismatch between the Pade approximation and the true time delay and the complex uncertainty $\Delta_{\tau_v}(s)$ s.t. $||\Delta_{\tau_v}(s)||_\infty \leq 1$ that models the variable time delay.

$$\begin{bmatrix} \mathbf{z}_\Delta \\ \mathbf{e}_{e_t} \\ \mathbf{e}_{u_D} \\ \mathbf{r} \\ \mathbf{y}_{S_n} \end{bmatrix} = \operatorname{diag}\left(\begin{array}{c} \mathbf{I} \\ \mathbf{W}_{e_t} \\ \mathbf{W}_{u_D} \\ \mathbf{I} \\ \mathbf{I} \end{array}\right) \left[\begin{array}{c|cc|c} \mathbf{G}_{z_\Delta w_\Delta} & \mathbf{0} & \mathbf{0} & \mathbf{G}_{z_\Delta u_D} \\ -\mathbf{G}_{y_S w_\Delta} & \mathbf{G}_{\text{ref}} & \mathbf{0} & -\mathbf{G}_{y_S u_D} \\ \mathbf{0} & \mathbf{0} & \mathbf{0} & \mathbf{I} \\ \hline \mathbf{0} & \mathbf{I} & \mathbf{0} & \mathbf{0} \\ \hline \mathbf{G}_{y_S w_\Delta} & \mathbf{0} & \mathbf{I} & \mathbf{G}_{y_S u_D} \end{array}\right]}_{\mathbf{P}_D} \operatorname{diag}\left(\begin{array}{c} \mathbf{I} \\ \mathbf{W}_r \\ \mathbf{W}_{n_S} \\ \mathbf{I} \end{array}\right) \begin{bmatrix} \mathbf{w}_\Delta \\ \mathbf{d}_r \\ \mathbf{d}_{n_s} \\ \mathbf{u}_D \end{bmatrix}. \tag{12}$$

$$\begin{bmatrix} \mathbf{z}_\Delta \\ \mathbf{e}_{e_t} \\ \mathbf{e}_{u_D} \end{bmatrix} = \operatorname{diag}\left(\begin{array}{c} \mathbf{I} \\ \mathbf{W}_{e_t} \\ \mathbf{W}_{u_D} \end{array}\right) \underbrace{\left[\begin{array}{c|cc} \mathbf{G}_{z_\Delta w_\Delta} + \mathbf{G}_{z_\Delta u_D}\mathbf{S}_{i_D}\mathbf{K}_S\mathbf{G}_{y_S w_\Delta} & \mathbf{G}_{z_\Delta u_\Delta}\mathbf{S}_{i_D}\mathbf{K}_r & \mathbf{G}_{z_\Delta u_\Delta}\mathbf{S}_{i_D}\mathbf{K}_S \\ -\left(\mathbf{I}+\mathbf{T}_{o_D}\right)\mathbf{G}_{y_S w_\Delta} & \mathbf{G}_{\text{ref}}-\mathbf{G}_{y_S u_D}\mathbf{S}_{i_D}\mathbf{K}_r & -\mathbf{T}_{o_D} \\ \mathbf{S}_{i_D}\mathbf{K}_S\mathbf{G}_{y_S w_\Delta} & \mathbf{S}_{i_D}\mathbf{K}_r & \mathbf{S}_{i_D}\mathbf{K}_S \end{array}\right]}_{\mathbf{M}_D=\mathcal{F}_l(\mathbf{P}_D,\mathbf{K}_D)} \operatorname{diag}\left(\begin{array}{c} \mathbf{I} \\ \mathbf{W}_r \\ \mathbf{W}_{n_S} \end{array}\right) \begin{bmatrix} \mathbf{w}_\Delta \\ \mathbf{d}_r \\ \mathbf{d}_{n_s} \end{bmatrix}. \tag{13}$$

$$\begin{bmatrix} \mathbf{z}_\Delta \\ \mathbf{z}_\tau \\ \mathbf{z}_{\tau_v} \\ \mathbf{e}_{y_L} \\ \mathbf{e}_u \\ \mathbf{y}_{C_n} \\ \mathbf{y}_{A_n} \end{bmatrix} = \operatorname{diag}\left(\begin{array}{c} \mathbf{I} \\ \mathbf{I} \\ \mathbf{I} \\ \mathbf{W}_{y_L} \\ \mathbf{W}_u \\ \mathbf{I} \\ \mathbf{I} \end{array}\right) \underbrace{\left[\begin{array}{ccc|cccc} \mathbf{G}_{z_\Delta w_\Delta} & \mathbf{0} & \mathbf{0} & \mathbf{G}_{z_\Delta r} & \mathbf{0} & \mathbf{0} & \mathbf{G}_{z_\Delta u} \\ \mathbf{G}_C\mathbf{G}_{y_L w_\Delta} & \mathbf{0} & \mathbf{0} & \mathbf{G}_C\mathbf{G}_{y_L r} & \mathbf{G}_C & \mathbf{0} & \mathbf{G}_C\mathbf{G}_{y_L u} \\ \mathbf{G}_\tau\mathbf{G}_C\mathbf{G}_{y_L w_\Delta} & \mathbf{I} & \mathbf{0} & \mathbf{G}_\tau\mathbf{G}_C\mathbf{G}_{y_L r} & \mathbf{G}_\tau\mathbf{G}_C & \mathbf{0} & \mathbf{G}_\tau\mathbf{G}_C\mathbf{G}_{y_L u} \\ \mathbf{G}_{y_L w_\Delta} & \mathbf{0} & \mathbf{0} & \mathbf{G}_{y_L r} & \mathbf{0} & \mathbf{0} & \mathbf{G}_{y_L u} \\ \mathbf{0} & \mathbf{0} & \mathbf{0} & \mathbf{0} & \mathbf{0} & \mathbf{0} & \mathbf{I} \\ \hline \mathbf{G}_\tau\mathbf{G}_C\mathbf{G}_{y_L w_\Delta} & \mathbf{I} & \mathbf{I} & \mathbf{G}_\tau\mathbf{G}_C\mathbf{G}_{y_L r} & \mathbf{G}_\tau\mathbf{G}_C & \mathbf{0} & \mathbf{I} & \mathbf{G}_\tau\mathbf{G}_C\mathbf{G}_{y_L u} \\ \mathbf{G}_{y_A w_\Delta} & \mathbf{0} & \mathbf{0} & \mathbf{G}_{y_A r} & \mathbf{0} & \mathbf{I} & \mathbf{0} \end{array}\right]}_{\mathbf{P}} \operatorname{diag}\left(\begin{array}{c} \mathbf{I} \\ \mathbf{W}_{\Delta_\tau} \\ \mathbf{W}_{\Delta_{\tau_v}} \\ \mathbf{W}_r \\ \mathbf{W}_{n_L} \\ \mathbf{W}_{n_A} \\ \mathbf{W}_{n_C} \\ \mathbf{I} \end{array}\right) \begin{bmatrix} \mathbf{w}_\Delta \\ \mathbf{w}_\tau \\ \mathbf{w}_{\tau_v} \\ \mathbf{d}_r \\ \mathbf{d}_{n_L} \\ \mathbf{d}_{n_A} \\ \mathbf{d}_{n_C} \\ \mathbf{u} \end{bmatrix} \tag{14}$$

$$\begin{bmatrix} \mathbf{z}_\Delta \\ \mathbf{z}_\tau \\ \mathbf{z}_{\tau_v} \\ \mathbf{e}_{y_L} \\ \mathbf{e}_u \end{bmatrix} = \operatorname{diag}\left(\begin{array}{c} \mathbf{I} \\ \mathbf{I} \\ \mathbf{I} \\ \mathbf{W}_{y_L} \\ \mathbf{W}_u \end{array}\right) \left[\begin{array}{c|c} \bar{\mathbf{M}}_{11} & \bar{\mathbf{M}}_{12} \\ \hline \bar{\mathbf{M}}_{21} & \bar{\mathbf{M}}_{22} \end{array}\right] \operatorname{diag}\left(\begin{array}{c} \mathbf{I} \\ \mathbf{W}_{\Delta_\tau} \\ \mathbf{W}_{\Delta_{\tau_v}} \\ \mathbf{W}_r \\ \mathbf{W}_{n_L} \\ \mathbf{W}_{n_A} \\ \mathbf{W}_{n_C} \end{array}\right) \begin{bmatrix} \mathbf{w}_\Delta \\ \mathbf{w}_\tau \\ \mathbf{w}_{\tau_v} \\ \mathbf{d}_r \\ \mathbf{d}_{n_L} \\ \mathbf{d}_{n_A} \\ \mathbf{d}_{n_C} \end{bmatrix}, \tag{15}$$

with

$$\bar{\mathbf{M}}_{11} = \left[\begin{array}{ccc} \mathbf{G}_{z_\Delta w_\Delta} + \mathbf{G}_{z_\Delta u}\mathbf{S}\left(\mathbf{K}_C\mathbf{G}_\tau\mathbf{G}_C\mathbf{G}_{y_L w_\Delta} + \mathbf{K}_A\mathbf{G}_{y_A w_\Delta}\right) & \mathbf{G}_{z_\Delta u}\mathbf{S}\mathbf{K}_C & \mathbf{G}_{z_\Delta u}\mathbf{S}\mathbf{K}_C \\ \mathbf{G}_C\left[\left(\mathbf{I}+\mathbf{T}\right)\mathbf{G}_{y_L w_\Delta} + \mathbf{S}\mathbf{K}_A\mathbf{G}_{y_A w_\Delta}\right] & \mathbf{G}_C\mathbf{G}_{y_L u}\mathbf{S}\mathbf{K}_C & \mathbf{G}_C\mathbf{G}_{y_L u}\mathbf{S}\mathbf{K}_C \\ \mathbf{G}_\tau\mathbf{G}_C\left[\left(\mathbf{I}+\mathbf{T}\right)\mathbf{G}_{y_L w_\Delta} + \mathbf{S}\mathbf{K}_A\mathbf{G}_{y_A w_\Delta}\right] & \mathbf{I}+\mathbf{T} & \mathbf{T} \end{array}\right], \tag{16}$$

$$\bar{\mathbf{M}}_{12} = \left[\begin{array}{cccc} \mathbf{G}_{z_\Delta r} + \mathbf{G}_{z_\Delta u}\mathbf{S}\left(\mathbf{K}_C\mathbf{G}_\tau\mathbf{G}_C\mathbf{G}_{y_L r} + \mathbf{K}_A\mathbf{G}_{y_A r}\right) & \mathbf{G}_{z_\Delta}\mathbf{S}\mathbf{K}_C\mathbf{G}_\tau\mathbf{G}_C & \mathbf{G}_{z_\Delta u}\mathbf{S}\mathbf{K}_A & \mathbf{G}_{z_\Delta u}\mathbf{S}\mathbf{K}_C \\ \mathbf{G}_C\left[\left(\mathbf{I}+\mathbf{T}\right)\mathbf{G}_{y_L r} + \mathbf{G}_{y_L u}\mathbf{K}_A\mathbf{G}_{y_A r}\right] & \mathbf{G}_C\left(\mathbf{I}+\mathbf{T}\right) & \mathbf{G}_C\mathbf{G}_{y_L u}\mathbf{S}\mathbf{K}_A & \mathbf{G}_C\mathbf{G}_{y_L u}\mathbf{S}\mathbf{K}_C \\ \mathbf{G}_\tau\mathbf{G}_C\left[\left(\mathbf{I}+\mathbf{T}\right)\mathbf{G}_{y_L r} + \mathbf{G}_{y_L u}\mathbf{K}_A\mathbf{G}_{y_A r}\right] & \mathbf{G}_\tau\mathbf{G}_C\left(\mathbf{I}+\mathbf{T}\right) & \mathbf{G}_\tau\mathbf{G}_C\mathbf{G}_{y_L u}\mathbf{S}\mathbf{K}_A & \mathbf{T} \end{array}\right], \tag{17}$$

$$\bar{\mathbf{M}}_{21} = \left[\begin{array}{ccc} \left(\mathbf{I}+\mathbf{T}\right)\mathbf{G}_{y_L w_\Delta} + \mathbf{G}_{y_L u}\mathbf{S}\mathbf{K}_A\mathbf{G}_{y_A w_\Delta} & \mathbf{G}_{y_L u}\mathbf{S}\mathbf{K}_C & \mathbf{G}_{y_L u}\mathbf{S}\mathbf{K}_C \\ \mathbf{S}\left(\mathbf{K}_C\mathbf{G}_\tau\mathbf{G}_C\mathbf{G}_{y_L w_\Delta} + \mathbf{K}_A\mathbf{G}_{y_A w_\Delta}\right) & \mathbf{S}\mathbf{K}_C & \mathbf{S}\mathbf{K}_C \end{array}\right], \tag{18}$$

$$\bar{\mathbf{M}}_{22} = \left[\begin{array}{cccc} \left(\mathbf{I}+\mathbf{T}\right)\mathbf{G}_{y_L r} + \mathbf{G}_{y_L u}\mathbf{S}\mathbf{K}_A\mathbf{G}_{y_A r} & \mathbf{T} & \mathbf{G}_{y_L u}\mathbf{S}\mathbf{K}_A & \mathbf{G}_{y_L u}\mathbf{S}\mathbf{K}_C \\ \mathbf{S}\left(\mathbf{K}_C\mathbf{G}_\tau\mathbf{G}_C\mathbf{G}_{y_L r} + \mathbf{K}_A\mathbf{G}_{y_A r}\right) & \mathbf{S}\mathbf{K}_C\mathbf{G}_\tau\mathbf{G}_C & \mathbf{S}\mathbf{K}_A & \mathbf{S}\mathbf{K}_C \end{array}\right], \tag{19}$$

The input filters $\mathbf{W}_r$, $\mathbf{W}_{n_L}$, $\mathbf{W}_{n_C}$ and $\mathbf{W}_{n_A}$ scale the amplitude spectrum of the reference $\mathbf{r}$ and of the sensor noises $\mathbf{n}_L$, $\mathbf{n}_C$ and $\mathbf{n}_A$.

According to Fig. 6, the general open-loop interconnection can be written as done for the DFSM control architecture as in (14).

If now $\mathbf{K} = \operatorname{diag}\left(\mathbf{K}_C, \mathbf{K}_A\right)$ is used to close the loop such that $\mathbf{u} = \mathbf{K}\begin{bmatrix} \mathbf{y}_{C_n} & \mathbf{y}_{A_n} \end{bmatrix}^{\mathrm{T}}$, define $\mathbf{S} = \left[\mathbf{I}+\mathbf{K}_C\mathbf{G}_\tau\mathbf{G}_C\mathbf{G}_{y_L u}\right]^{-1}$ and $\mathbf{T} = \mathbf{I} - \mathbf{S}$ as the sensitivity and the complementary sensitivity functions. Since the feedback is a single input single output channel (SISO) the output sensitivity and the output complementary sensitivity functions are the same as the input

functions. The closed-loop interconnection matrix $\mathbf{M} = \left[\begin{array}{c|c} \mathbf{M}_{11} & \mathbf{M}_{12} \\ \hline \mathbf{M}_{21} & \mathbf{M}_{22} \end{array}\right] = \mathcal{F}_l(\mathbf{P},\mathbf{K})$, where $\mathcal{F}_l$ with $\mathbf{M}_{kj} = \mathbf{P}_{kj} + \mathbf{P}_{k3}\mathbf{S}_i\mathbf{K}\mathbf{P}_{3j}$, takes the form (15).

2) Weighting functions selection: The uncertainty weights $\mathbf{W}_{\Delta_\tau}$ and $\mathbf{W}_{\Delta_{\tau_v}}$, used for the CCD camera model, scale the blocks $\mathbf{M}_{11}$ and $\mathbf{M}_{21}$. Any increase in the weights, covering a larger uncertainty set, must be accompanied by a corresponding decrease in the maximum gains of some closed-loop functions, such as $\mathbf{T}$ and $\mathbf{S}\mathbf{K}_C$, that are scaled by that particular weight. At the same time the functions $\mathbf{S}\mathbf{K}_C$ and $\mathbf{T}$ also appear in the closed-loop transfer function $\mathbf{d} \to \mathbf{e}_{y_L}$. To maximize the performances
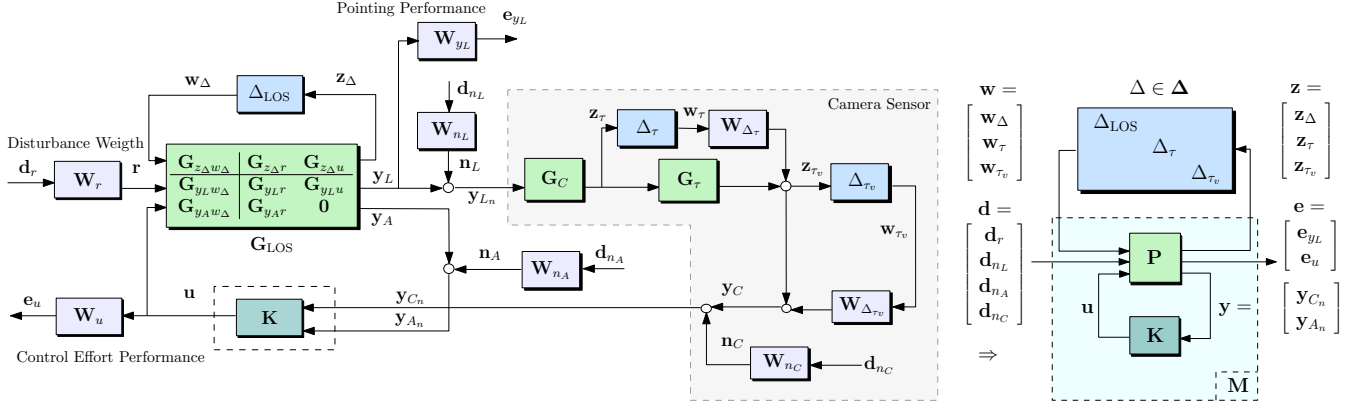
Fig. 6. Interconnection structure for robust synthesis and analysis of the LOS stabilization subsystem.

on the disturbance rejection, it is thus necessary to use the smallest set of uncertainty to model the fixed and variable time delay using low magnitude weights.

The weighting function $\mathbf{W}_{\Delta_\tau}$ scales the additive complex uncertainty in order to compensate for the 2nd-order Pade approximation used to model the fixed time delay of the CCD camera. A 4th-order Butterworth high-pass filter $\mathbf{B}_{hp}$ with cut-off frequency at $83\,\mathrm{Hz}$ and low-frequency gain $\alpha = 2$ is used to fit the difference between the true time delay and the Pade approximation $\mathbf{W}_{\Delta_\tau}$:

$$\mathbf{W}_{\Delta_\tau} = \alpha \cdot \mathbf{B}_{hp}. \tag{20}$$

The weighting function $\mathbf{W}_{\Delta_{\tau_v}}$ provides an overbound on the multiplicative uncertainty used to model the CCD variable time delay $\tau_v \in [0, \tau_{v_{\max}}]$. The model proposed by Wang *et al.* [41] is used:

$$\mathbf{W}_{\Delta_{\tau_v}} = \frac{s}{1/3.465s + \tau_{v_{\max}}^{-1}}, \tag{21}$$

with $\tau_{v_{\max}} = 1\,\mathrm{ms}$.

The input weight $\mathbf{W}_r$ is scaled on the maximum expected amplitude spectrum input of the disturbance signal spectrum with a 2nd-order low-pass Butterworth filter with cut-off frequency $\omega_{\mathrm{co}} = 2\pi \cdot 100\,\mathrm{rad/s}$:

$$\mathbf{W}_r = \frac{\beta \omega_{\mathrm{co}}^2}{s^2 + 1.4121\omega_{\mathrm{co}}s + \omega_{\mathrm{co}}^2} \tag{22}$$

with $\beta = 7\%$.

The input weights $\mathbf{W}_{n_L}$, $\mathbf{W}_{n_A}$ used to scale the sensor noises from the autocollimator and the ARS are directly provided by the identification phase as explained in Section II-B at step 5. These filters are shown in Fig. 5b and Fig. 5c respectively. For the CCD model noise, a 3rd-order high-pass filter $\mathbf{W}_{n_C}$ in (23) with low-frequency gain of $32.321\,\mathrm{nrad}$ is chosen after analysis of real spacecraft scenario:

$$\mathbf{W}_{n_C} = 32.321 \cdot 10^{-3} \cdot \left(\frac{s + 2\pi \cdot 9.4872}{s + 10 \cdot 2\pi \cdot 9.4872} \right)^3 \tag{23}$$

With the uncertainty and input weights properly set the output weighting functions $\mathbf{W}_{y_L}$ and $\mathbf{W}_u$ translate the performance requirement (**R2**) at Section II-D. Their

inverse indeed represent the desired worst-case upper bound on the amplitude spectra of the absolute LOS jitter and the normalized actuator control signal. According to $\mathbf{W}_u$ a unit gain filter is used, that imposes an upper bound on the normalized amplitude spectrum of the control input. This maximum amplitude corresponds to the operational amplitude voltage range provided by the manufacturer with guaranteed performances of the device without encountering any degradation. The performance filter on input disturbances rejection $\mathbf{W}_{y_L}$ shapes both the sensitivity function $\mathbf{S}$ and the complementary sensitivity function $\mathbf{T}$ as shown in (19) in the transfer function $\bar{\mathbf{M}}_{22}$. This architecture is a particular case of tracking problem where the reference is 0. As a consequence, to have a high rejection a high gain of $\mathbf{T}$ has to be imposed in the bandwidth of interest. However this high gain also implies a high level of autocollimator sensor noise in the same bandwidth and therefore limits the pointing performance (see transfer function $\mathbf{d}_{n_L} \to \mathbf{e}_{y_L}$ in (19)).

Three different controllers were studied in order to highlight the advantages to make the fusion of the CCD and ARS measurements:

1) **Scenario 1**: only CCD measurements available;
2) **Scenario 2**: only ARS measurements available;
3) **Scenario 3**: both CCD and ARS measurements available.

According to the previous considerations $\mathbf{W}_{y_L}$ were chosen differently according to the three different scenarios.

For Scenario 1 a 4th-order Butterworth low-pass filter $\mathbf{B}_{lp}^i$ with cut-off frequency of $9\,\mathrm{Hz}$ and low-frequency gain of $1/\varepsilon_{\max}$ is chosen, with $\varepsilon_{\max} = 10\,\mu\mathrm{rad}$ upper bound on the accepted LOS jitter spectrum amplitude:

$$\mathbf{W}_{y_L}^i = (1/\varepsilon_{\max}) \cdot \mathbf{B}_{lp}^i \tag{24}$$

This filter imposes a closed-loop upper bound on the LOS spectrum of $10\,\mu\mathrm{rad}$ up to a frequency of $9\,\mathrm{Hz}$. This is a conservative requirement since only low frequency signals from the virtual CCD are made available.

For Scenario 2 a 4th-order band-pass Butterworth filter $\mathbf{B}_{bp}$ is used with low frequency cut-off frequency of $10\,\mathrm{Hz}$ and high frequency cut-off frequency of $100\,\mathrm{Hz}$. The

Butterworth filter $\mathbf{B}_{bp}$ is built so as not to demand a low LOS jitter where the ARS transfer function has a low gain at low frequency and beyond the rejection bandwidth of interest. The low frequency gain is imposed at $1/\varepsilon_{\max}$ and a Notch filter $\mathbf{N}$ is added to compensate for the electric noise caused by the main supply voltage at 50 Hz:

$$\mathbf{W}_{y_L}^{ii} = (1/\varepsilon_{\max}) \cdot \mathbf{B}_{bp} \cdot \mathbf{N} \qquad (25)$$

where $\mathbf{N} = \frac{s^2 + 2\gamma_{\min}\zeta\omega_{NF}s + \omega_{NF}^2}{s^2 + 2\zeta\omega_{NF}s + \omega_{NF}^2}$, with $\gamma_{\min} = -30\,\mathrm{dB}$, $\zeta = 0.1$ and $\omega_{NF} = 2\pi \cdot 50\mathrm{rad/s}$.

Finally for Scenario 3 a 4th-order Butterworth low-pass filter $\mathbf{B}_{lp}^{iii}$ with cut-off frequency of 100 Hz together with a low frequency gain of $1/\varepsilon_{\max}$ and the Notch filter $\mathbf{N}$:

$$\mathbf{W}_{y_L}^{iii} = (1/\varepsilon_{\max}) \cdot \mathbf{B}_{lp}^{iii} \cdot \mathbf{N} \qquad (26)$$

E. Control synthesis

Both control syntheses for the DFSM and CFSM follow the same problem formulation. The notation for CFSM will be used in this section but the same conclusions have to be associated with the DFSM problem. The controller synthesis is thus expressed as a multicriteria optimization problem on the closed-loop transfer function $\mathbf{M} = \mathcal{F}_l(\mathbf{P}, \mathbf{K})$:

$$
\begin{aligned}
&\underset{\substack{\mathbf{K}\in\mathcal{K},\\ \{\mathcal{D}_S,\mathcal{D}_1,\dots,\mathcal{D}_n\}\in\mathbb{D}}}{\text{minimize}} \quad \gamma \quad \text{s.t.} \\
&\left\{ \begin{array}{l} \left\|\mathcal{D}_S\mathbf{M}_{11}\mathcal{D}_S^{-1}\right\|_\infty < 1/\nu \\ \left\|\mathrm{diag}\left(\begin{bmatrix} \mathcal{D}_i\sqrt{\epsilon} & \\ & \mathcal{X}_i \end{bmatrix} \mathbf{M} \begin{bmatrix} \sqrt{\epsilon}\mathcal{D}_i^{-1} & \\ & \mathbf{I} \end{bmatrix} \right)\right\|_\infty < \gamma \end{array} \right., \\
&i \in \{1,\dots,n\},
\end{aligned}
$$
$$(27)$$

with $\mathcal{X}_i = \begin{bmatrix} \mathbf{0}_{1\times(i-1)} & 1 & \mathbf{0}_{1\times(n-i)} \end{bmatrix}$. Here, $\mathcal{D}_\bullet$ are the so-called D-scaling matrices so that, for any $\mathcal{D}_\bullet \in \mathbb{D}$ and $\Delta \in \mathbf{\Delta}$, the condition $\mathcal{D}_\bullet\Delta = \Delta\mathcal{D}_\bullet$ holds [42]. In order to increase the number of degrees of freedom, the level of guaranteed robust performance, different D-scales are used for the robust stability and robust performance conditions in (27). The constraint $\left\|\mathcal{D}_S\mathbf{M}_{11}\mathcal{D}_S^{-1}\right\|_\infty < 1/\nu$ is used to impose the robust stability condition (**R1**) for any uncertainty $\Delta \in \mathbf{\Delta}$ with $\|\Delta\|_\infty < \nu$. The subsequent constraints are used to enforce each of the robust performance requirements (**R2**) for $\|\Delta\|_\infty < \epsilon/\gamma$, where $\epsilon \in [0,1]$ tunes the trade-off between performance and robustness (see [11] for details). The NP-hard problem (27) is classically solved with the DK-iteration algorithm [33], which provides a high order controller (*unstructured controller*). This approach is used in this work to initialize the controller and the D-scales for solving (27) in order to obtain a *structured* low-order and robust controller with modern nonsmooth $\mathcal{H}_\infty$ synthesis techniques [28], [29]. The optimization strategy used in this work is described in further detail in the following four steps:

Step 1: The original minimization problem given in (27) is reduced to the simpler, but more conservative, single criteria optimization:

$$
\begin{aligned}
&\underset{\bar{\mathbf{K}}\in\mathcal{K},\bar{\mathcal{D}}\in\mathbb{D}}{\text{minimize}} \quad \gamma \quad \text{s.t.} \\
&\left\|\begin{bmatrix} \bar{\mathcal{D}}\sqrt{\epsilon} & \\ & \mathbf{I} \end{bmatrix} \mathbf{M} \begin{bmatrix} \sqrt{\epsilon}\bar{\mathcal{D}}^{-1} & \\ & \mathbf{I} \end{bmatrix}\right\|_\infty < \gamma,
\end{aligned}
$$
$$(28)$$

with fixed $\bar{\mathcal{D}}$ and ϵ. This problem is solved with the classical DK-iteration algorithms that provide an unstructured controller that has the same order of the augmented plant $\mathbf{P}$.

Step 2: Model reduction of the set $\mathcal{D}$ obtained at Step 1 by balanced stochastic model truncation (BST) via Schur method [43], [44] to a lower order. A 2nd-order transfer function is generally used.

Step 3: Model reduction of the controller $\bar{\mathbf{K}}$ obtained at Step 1 by BST to get a structured low order controller $\mathbf{K}$.

Step 4: The D-scale matrices obtained at Step 2 and the controller $\mathbf{K}$ obtained at Step 3 are used to initialize and solve the full minimization problem (27). As this problem is less conservative and with more degrees of freedom compared with (28), it follows that the performances are guaranteed to improve.

III. RESULTS AND DISCUSSION

In this section the results of the identification and control will be given both for the DFSM and for the complete LOS stabilization bench. Then a practical application for the LOS stabilization of a spacecraft will be outlined.

A. Disturbing Fast Steering Mirror: identification and control

The DFSM is a tip/tilt platform the axes of which can be decoupled and considered as a SISO system. The results of the system identification described in Section II-B for the DFSM are shown in Fig.7. The nominal DFSM transfer function between the input voltage $\mathbf{u}_D$ and the strain gauge voltage $\mathbf{y}_S$ is identified as a third order. The filter $\mathbf{W}_{\Delta_D}$ used to scale the additive uncertainty on the plant (see Section II-B step 7) is shown in Fig. 7b. This filter has a two-poles two-zeros transfer function. The strain gauge sensor noise $\mathbf{n}_S$ is shown in Fig. 5a and is modeled as a constant gain $\mathbf{W}_{n_S}$ multiplying the normalized noise $\mathbf{d}_r$.

The structure of the controller is obtained by a reduction to a fourth-order model of the unstructured controller (see Section II-E at step 3). The experimental closed-loop validation is shown in Fig. 8. The experimental results are consistent with the predicted results and the controller makes it possible to extend the unit gain transfer up to 100 Hz with phase recovery of 180° on the same bandwidth as demanded by (**R2**) in Section II-C.
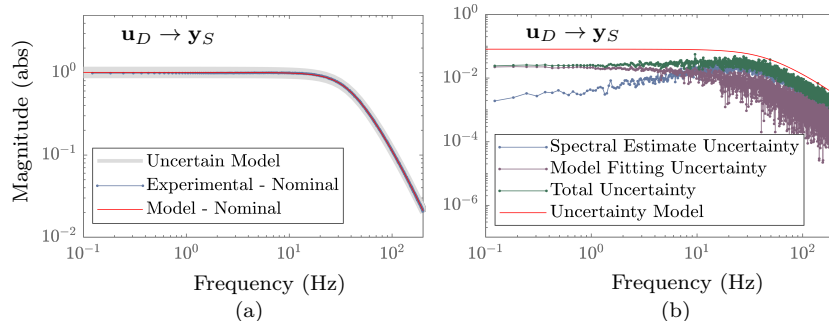
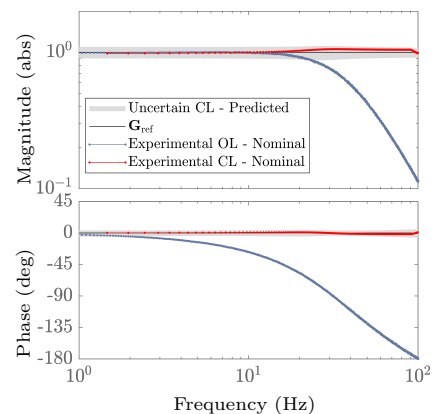Fig. 7. DFSM identification: (a) Transfer function model, (b) Uncertainty model.

Fig. 8. DFSM closed loop validation.

B. LOS stabilization bench: identification and control

Once the DFSM control is validated, the entire LOS stabilization bench is identified with the DFSM in closed-loop as shown in Fig. 2. The reference signal $\mathbf{r}$ is the same chirp signal used for the identification of the DFSM setup. The results of the identification procedure are summarized in Fig. 9. The autocollimator and the ARS noises are respectively shown in Fig. 5b and Fig. 5c. The ARS measurements are affected at 50 Hz by significant electrical noise due to the main power supply. It impacts the model of the transfer function $\mathbf{r} \to \mathbf{y}_A$ (see Fig. 9) that is highly uncertain at 50 Hz, where the coherence spectrum (6) is poor.

For the three scenarios, a structured controller with 8 states is chosen. For the scenario where CCD and ARS measurements are available $\mathbf{K}_C$ and $\mathbf{K}_A$ both have 8 states.

1) Robust stability and worst-case analysis: For this analysis only **Scenario 1** and **Scenario 3** are considered since **Scenario 2** with only ARS measurements is a pure feed-forward that can never destabilize the system. The computation of the structured singular value $\mu_\Delta (\mathbf{M}_{11})$, numerically performed here by the MATLAB function *robstab* [45], provides the stability margin of the closed loop interconnection with respect to the set of uncertainty $\Delta \in \mathbf{\Delta}$. The impact of each uncertainty of the set $\mathbf{\Delta}$ on the stability margin can be studied separately in order to check the sensitivity of certain parameters on stability robustness. The results of this analysis are synthesized in Fig. 10. Note that the peak values are all lower than one for each case, that means that the stability of the system is guaranteed for all uncertainty blocks. When only CCD measurements are available (Fig. 10a) the additive uncertainty on the CCD fixed time delay Δ_τ and the multiplicative uncertainty on the CCD variable time delay Δ_{τ_v} play the major role with respect to the full complex system uncertainty Δ_{LOS} at high frequency beyond the CCD bandwidth. When ARS measurements are also available (Fig. 10b) the stability margins are considerably improved on the whole bandwidth of interest. The biggest

degradation appears at 50 Hz, where the ARS electric noise is introduced in the closed-loop interconnection. Also in this case the CCD delays are the biggest contributors to margin degradation.

The high stability margins performed when the ARS is introduced as high frequency sensor suggest that the model of the camera variable time delay can be neglected or a bigger value of $\tau_{v_{max}}$ can be tolerated. This is not the case if only a CCD camera is used as LOS sensor.

The degradation of the performances with respect to the two indicators (rejection and control effort requirements) can be studied in the same framework. This is done by computing the upper bound of the structured singular value $\sup_\omega \mu_\Delta (\mathbf{M}_{\mathbf{d} \to \mathbf{e}_\bullet})$ from all the input disturbances $\mathbf{d}$ to each performance index: $\mathbf{e}_{y_L}$ for the rejection and $\mathbf{e}_u$ for the control effort. This analysis is numerically performed by the MATLAB function *wcgain* [45]. The results of this computation are shown in Fig. 11 for the three scenarios. In the three cases, the rejection index $\mathbf{e}_{y_L}$ is the one limiting the performances. The worst-case $\mathcal{H}_\infty$ gain for the two closed-loop performances of the transfer function $\mathbf{d} \to \mathbf{e}_\bullet$ with respect to the normalized complex uncertainty $\sup_{\Delta \in \mathbf{\Delta}, ||\Delta||_\infty < 1} ||\mathcal{F}_u(\mathbf{M}, \Delta)_{\mathbf{d} \to \mathbf{e}_\bullet}||_\infty$ remains everywhere below unity meaning that the performance requirements are robustly met in presence of the uncertainty set $\mathbf{\Delta}$.

2) Closed-loop validation and experimental results: The experimental closed-loop performances are compared in Fig. 12 with the predicted performances with respect to the rejection and control effort performance. The worst-case closed-loop performance over all frequencies is directly obtained from the analysis of the previous section. As shown in Fig. 12 the system is robust to the set of uncertainties for all three scenarios.

The advantage of the multi-sensor fusion of the CCD and ARS measurements is finally depicted in Fig.13, where rejection efficiency is normalized with respect to the open-loop performances. For the three scenarios a rejection of at least 13 dB is guaranteed (with exception of the notch at 50 Hz) on the respective bandwidths of interest. This performance is then reached on a 100 Hz bandwidth when
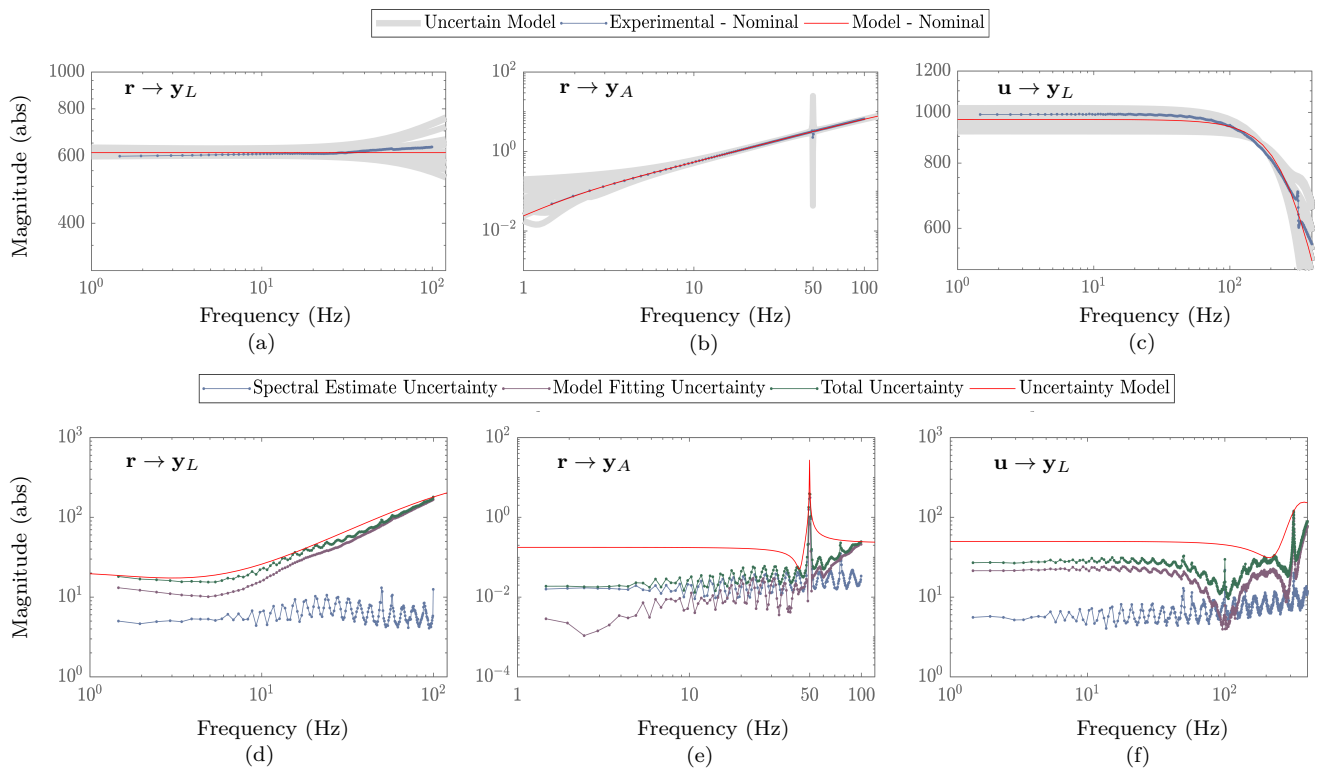
Fig. 9. LOS stabilization Identification: (a-c) Transfer function models, (d-f) Uncertainty models.
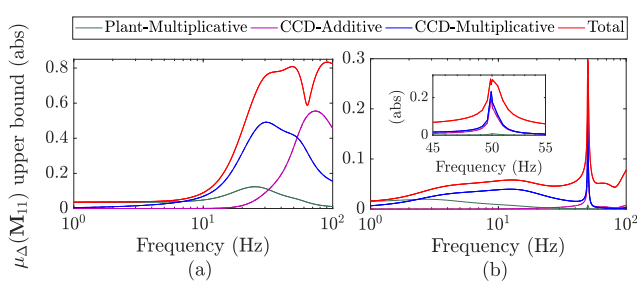

Fig. 10. Upper bound on $\mu_\Delta(\mathbf{M}_{11})$, which is the inverse robust stability margin, by considering separately the contribution given by the different uncertainty structures of the system and then the full set: (a) only CCD measurements available, (b) both CCD and ARS measurements available.
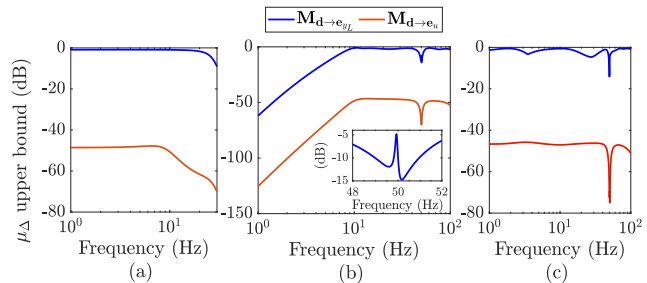
Fig. 11. Performance worst-case analysis. Upper bound on $\mu_\Delta\left(\mathbf{M}_{\mathbf{d}\to\mathbf{e}_{y_L}}\right)$ (blue lines) and $\mu_\Delta\left(\mathbf{M}_{\mathbf{d}\to\mathbf{e}_u}\right)$ (red lines): (a) only CCD measurements available, (b) only ARS measurements available, a zoom reveals a pick at 50 Hz (c) both CCD and ARS measurements available.

both CCD and ARS are used. The experimental results show even better performances with more than 20 dB of rejection between 2 and 50 Hz when sensor fusion is employed. The loss of performance at 50 Hz comes directly for the ARS electrical noise as already discussed in the previous sections. It has to be pointed out that this is only a laboratory limit since an AC main power supply is used. For Space application this limit is overcome by using a continuous power source.

C. LOS stabilization of a spacecraft: an application

The experimental setup presented in this article allows the user to test realistic spacecraft scenarios. The signal $\mathbf{r}$ in Fig. 2 can in fact be produced by a real mission LOS report or by a spacecraft model. The test bench can

then simulate the impact of an active control system for microvibrations reduction.

A schematic view of the system considered is shown in Fig. 14. A simple dynamic model of a flexible spacecraft is obtained thanks to recent development of the Satellite Dynamics Toolbox (SDT) [46]. The spacecraft taken into account has a flexible solar array driven by a SADM and a reaction wheel controlling the satellite axis pointing towards Earth. In the spacecraft block the coupled dynamics of the rigid main body with the flexible solar panel is described. The spacecraft inputs are the control torques $\mathbf{T}_{\text{ACS}}$ provided by the Attitude Control System (ACS). The considered disturbances are the RWA disturbances $\mathbf{d}_{\text{RWA}}$ together with the torque SADM torque T_{SADM} acting on the solar array.

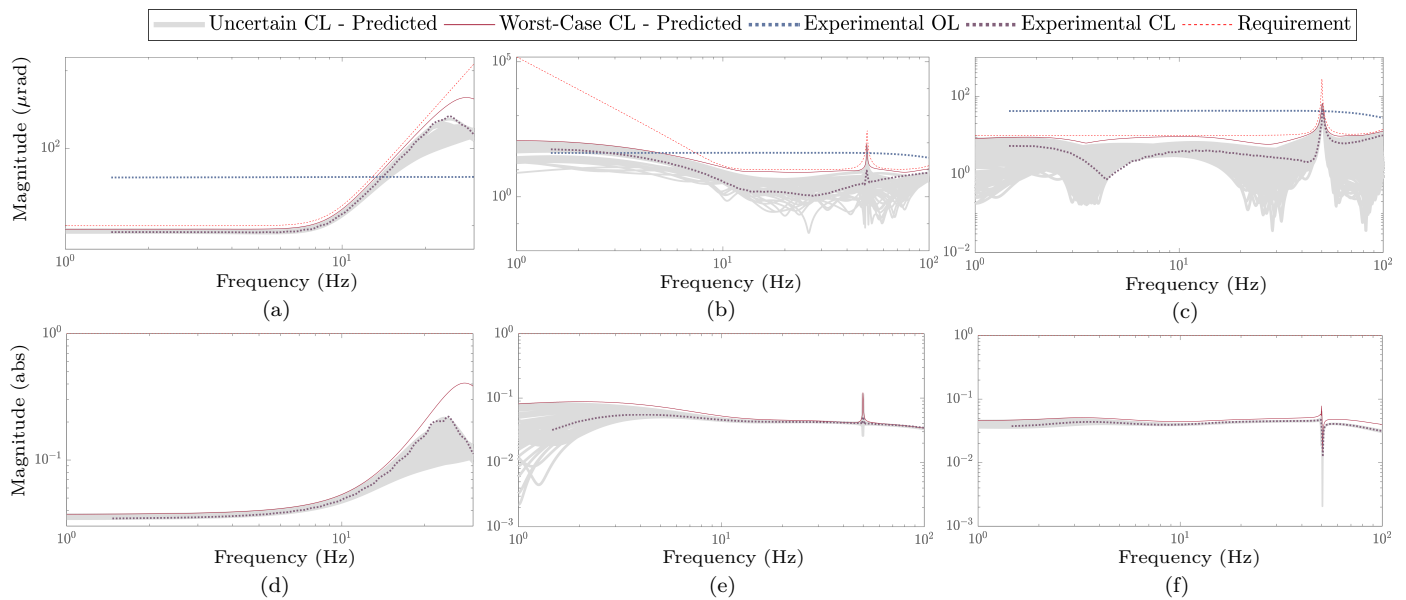The SADM block (permanent magnet stepper motor

Fig. 12. Closed loop validation - Robust rejection requirement: (a) only CCD measurements available, (b) only ARS measurements available, (c) both CCD and ARS measurements available; Control effort requirement: (d) only CCD measurements available, (e) only ARS measurements available, (f) both CCD and ARS measurements available.
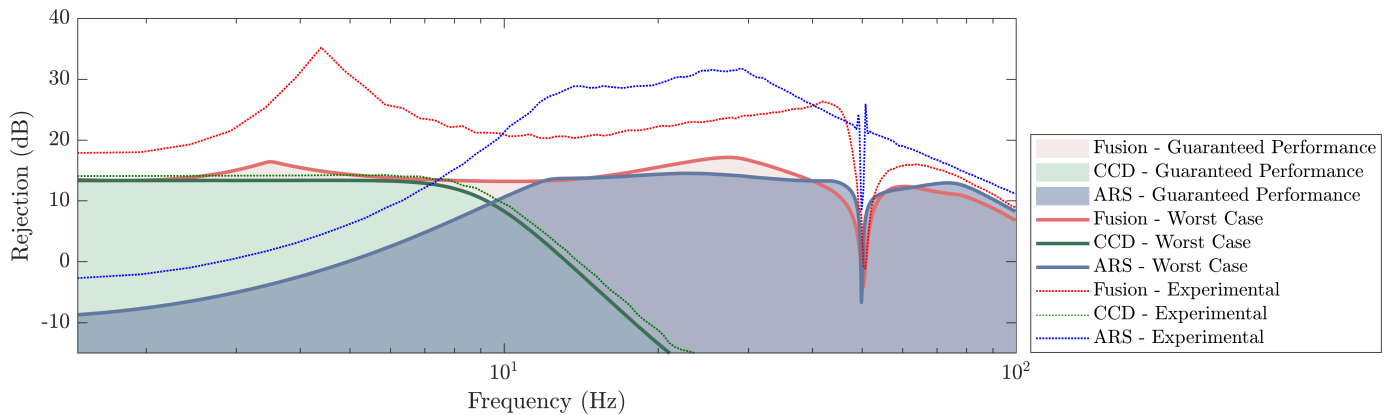

Fig. 13. Worst-case analysis and experimental results for rejection of microvibrations.
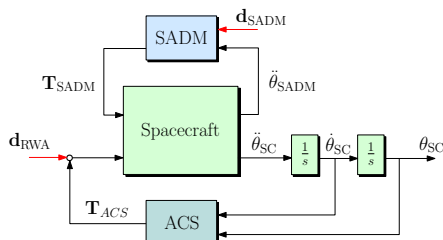

Fig. 14. Spacecraft control diagram.

with reduction gearbox) takes as input the current angular acceleration of the motor shaft $\ddot{\theta}_{SADM}$ and the reference stepped signal provided by an electronic driver $\mathbf{d}_{SADM}$, and provides the torque $\mathbf{T}_{SADM}$ acting on the solar array.

The spacecraft outputs are the acceleration of the entire system $\ddot{\boldsymbol{\theta}}_{SC}$ with respect to its center of mass, which provides the LOS jitter $\boldsymbol{\theta}_{SC}$ that is used as reference for the

experimental system and the acceleration of the SADM rotor shaft $\ddot{\boldsymbol{\theta}}_{SADM}$. The data used for the simulation are summarized in Table I.

For this particular example, the following assumptions were made:

1) The internal model of the reaction wheel dynamics (dependent on wheel speed) is not taken into account in order to simplify the study by neglecting the gyroscopic effect on the flexible modes migrations. For further details on this subject the reader is invited to refer to the works [10], [11].

2) The wheel introduces the disturbances $\mathbf{d}_{RWA}$ due to their mass unbalances and bearing imperfections. As already stated, these disturbances have an harmonic nature and they depend on the flywheel angular speed. They can be summed up in two forces and two torques components in the perpendicular axes to the flywheel rotational z-axis [8]:

TABLE I
Spacecraft parameter values

System	Parameter	Description	Value
Spacecraft main body	m_{SC}	Mass	$100\,\text{kg}$
	$\left[J_x^{\text{SC}}\,J_y^{\text{SC}},J_z^{\text{SC}}\right]$	Inertia in Spacecraft body frame	$[10\ 10\ 20]\,\text{kg}\cdot\text{m}^2$
Solar Array	m_{SA}	Mass	$50\,\text{kg}$
	$\left[J_x^{\text{SA}}\,J_y^{\text{SA}}\,J_z^{\text{SA}}\right]$	Inertia w.r.t. the SA reference frame	$[10\ 15\ 20]\,\text{kg}\cdot\text{m}^2$
	$\left[\omega_1^{\text{SA}}\,\omega_2^{\text{SA}}\,\omega_3^{\text{SA}}\right]$	Frequency of the flexible modes	$[0.8\ 15\ 40]\,\text{Hz}$
	$\zeta_1^{\text{SA}},\zeta_2^{\text{SA}},\zeta_3^{\text{SA}}$	Damping factor of the flexible modes	0.03
	$\mathbf{L}_{\text{SA}}$	Modal participation factors	$\begin{bmatrix} 3.536 & 3.536 & 0 & 0 & 0 & 0 \\ 0 & 3.536 & 3.536 & 0 & 0 & 0 \\ 0 & 0 & 0 & 0 & 0 & 3.162 \end{bmatrix}$
Reaction Wheel	$\boldsymbol{\Omega}$	Flywheel spin range	$[5,\ 50]\,\text{Hz}$
	$\left[C_1^f\,C_2^f\,C_3^f\,C_4^f\right]$	Multi-harmonic force coefficients	$[4.296\ 1.633\ 0.425\ 0.567]\cdot 10^{-3}\,\text{N}/(\text{rad/s})^2$
	$\left[C_1^t\,C_2^t\,C_3^t\,C_4^t\right]$	Multi-harmonic torque coefficients	$[1.772\ 0.407\ 0.169\ 0.066]\cdot 10^{-3}\,\text{N}\cdot\text{m}/(\text{rad/s})^2$
	$[h_1\,h_2\,h_3\,h_4]$	Harmonic numbers	$[1\,2\,3\,4]$
Solar Array Drive Mechanism	C_{S}	Harmonic torque coefficient	$0.57\,\text{N}\cdot\text{m}$
	z_{S}	Number of rotor teeth	90
	p_{S}	Number of motor poles	4
	n_{MS}	Number of micro-step subdivisions	8
	Ω_{S}	Rotor angular speed	$1\cdot 10^{-3}\,\text{rad/s}$
Attitude Control System	ω_{ACS}	Desired ACS bandwidth	$0.1\,\text{rad/s}$
	ζ_{ACS}	Desired ACS damping ratio	0.7

$$\mathbf{d}_{\text{RWA}} = \begin{bmatrix} \mathbf{F}_x \\ \mathbf{F}_y \\ \mathbf{T}_x \\ \mathbf{T}_y \end{bmatrix} = \Omega^2 \sum_{i=1}^{n_h} \begin{bmatrix} -C_i^f \sin(h_i\Omega t + \phi_i^f) \\ C_i^f \cos(h_i\Omega t + \phi_i^f) \\ C_i^t \cos(h_i\Omega t + \phi_i^t) \\ C_i^t \sin(h_i\Omega t + \phi_i^t) \end{bmatrix} \tag{29}$$

where C_i is the amplitude of the i-th harmonic, Ω is the flywheel angular speed, h_i is the harmonic number and ϕ_i is a random phase number such that $\phi \in [0, 2\pi]$.

3) The input signal $\mathbf{d}_{\text{SADM}}$ to the SADM dynamics contains only the high frequency disturbance provided by the micro-steps with respect to an ideal sinusoidal reference. It is assumed that the SADM is in stationary condition and that the low-frequency content of the torque introduced into the system is already compensated by the ACS. The SADM disturbance is assumed to be harmonic and depends on the rotor speed Ω_{S}:

$$\mathbf{d}_{\text{SADM}} = C_{\text{S}} \sin\left(z_{\text{S}} p_{\text{S}} n_{\text{MS}} \Omega_{\text{S}} t\right) \tag{30}$$

where C_{S} is the amplitude of the SADM disturbance harmonic, z_{S} the number of rotor teeth, p_{S} the number of poles and n_{MS} the number of micro-step divisions.

4) For simplicity reasons, the mirror is assumed to be rigidly connected to the spacecraft body. As such, the LOS errors are only induced by the attitude errors of the entire spacecraft $\boldsymbol{\theta}_{\text{SC}}$. Furthermore, the measurement from the ARS corresponds to the angular rate $\dot{\boldsymbol{\theta}}_{\text{SC}}$. In this case, the reference signal sent to the DFSM was chosen as the attitude $\boldsymbol{\theta}_{\text{SC}}$. For a more realistic scenario, the flexibility of the mirror should also be considered by taking into account the relative dynamics between the mirror and the rigid body of the spacecraft.

The ACS control torques are produced by three decoupled PD controllers tuned on the total static inertia of the spacecraft $\mathbf{J}^{\text{tot}}$:

$$\mathbf{T}_{\text{ACS}} = -\mathbf{K}_V \dot{\boldsymbol{\theta}}_{\text{SC}} - \mathbf{K}_P \boldsymbol{\theta}_{\text{SC}}, \tag{31}$$

with $\mathbf{K}_P = \omega_{\text{ACS}}^2 \cdot \text{diag}\left(J_x^{\text{tot}}, J_y^{\text{tot}}, J_z^{\text{tot}}\right)$ and $\mathbf{K}_V = 2\zeta_{\text{ACS}}\omega_{\text{ACS}} \cdot \text{diag}\left(J_x^{\text{tot}}, J_y^{\text{tot}}, J_z^{\text{tot}}\right)$, where ω_{ACS} and ζ_{ACS} are respectively the desired closed-loop bandwidth and the damping ratio.

The spacecraft is subsequently subjected to a slowly varying torque signal that induces a counter acting wheel speed variation within the range $\boldsymbol{\Omega} = [5, 50]\,\text{rev/s}$. The computed attitude error signal $\boldsymbol{\theta}_{\text{SC}}$ is subsequently used to drive the DSFM. Fig. 15 shows the amplitude spectrum and the cumulative root mean square spectrum of this signal. It can be seen that as the wheel is accelerated, the RWA harmonic perturbations given in (29) interact with the various flexible modes of the spacecraft around $5\,\text{Hz}$, $26.3\,\text{Hz}$ and $45.7\,\text{Hz}$. The peak at $88.32\,\text{Hz}$ corresponds to SADM excitation (30).

The controller was synthesized following the procedure presented in the previous section and uses both the CCD camera and ARS measurements. In this case, the disturbance weight $\mathbf{W}_r$ corresponds to an upper bound on the peak amplitude spectrum of the attitude error. With this reference weight in place, worst-case predictions of the LOS spectrum in closed-loop were made. The experimental closed-loop rejection results together with the worst-case predictions are shown in Fig. 16. As predicted, the experimental closed-loop performance remains below the requirement.
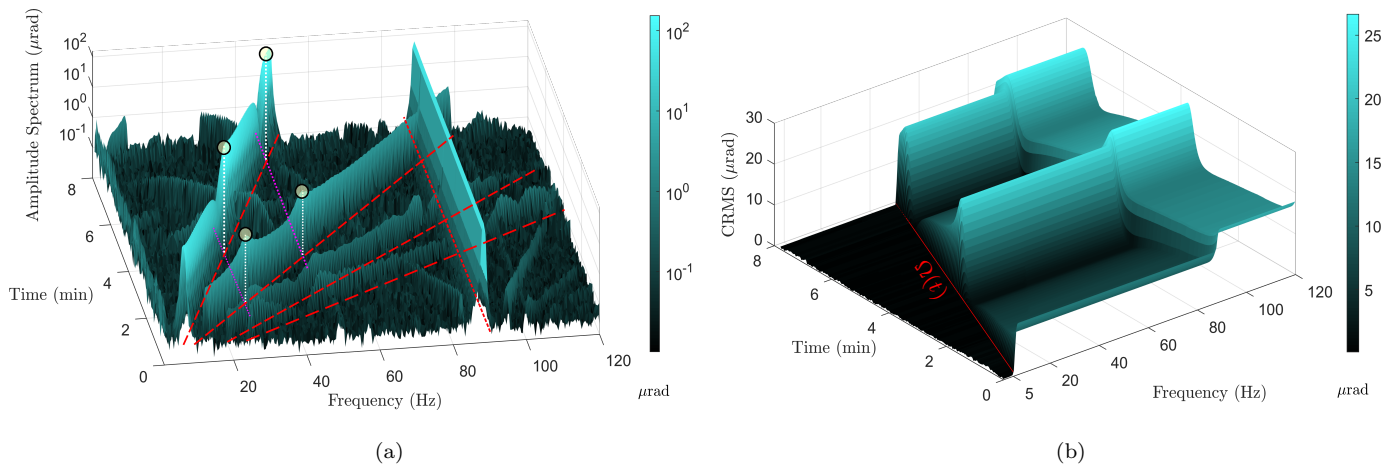
(a)

(b)

Fig. 15. (a) Amplitude Spectrum of the LOS: reaction wheel harmonics (dashed red lines), SADM harmonic (dotted red line), frequencies of spacecraft flexible modes (dotted purple line), interactions of reaction wheel harmonics with spacecraft flexible modes (yellow bullets) (b) CRMS of the LOS.
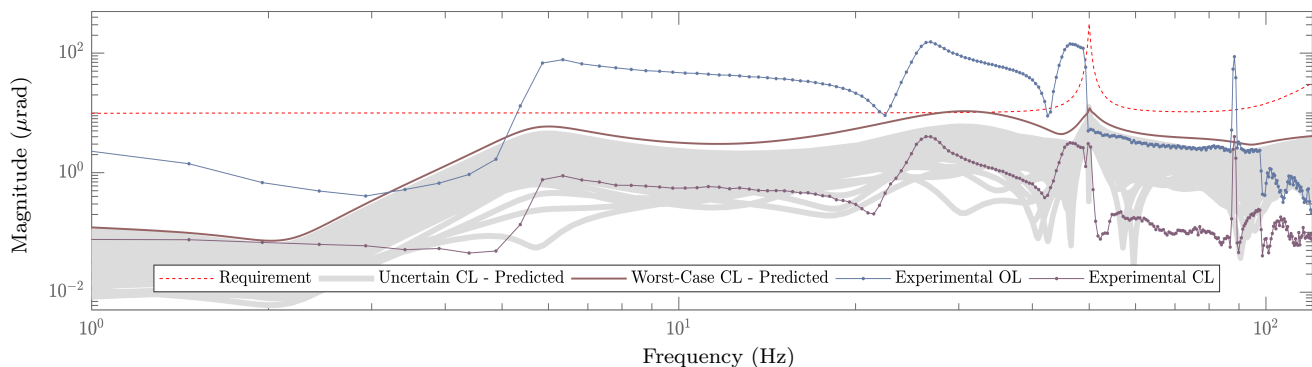

Fig. 16. Spacecraft LOS robust rejection performance in closed-loop.

This brief application shows as many other different experiments can be performed on the same test bench to study a variety of spacecraft platforms and/or simulate different optical sensitive payloads.

IV. Conclusions

This paper presents a robust line-of-sight stabilization method for high pointing accuracy Space missions. The core concept is based on combining measurements from a low frequency imaging system together with high frequency information from an angular rate sensor attached to the main line-of-sight disturbance source. The design methodology is demonstrated on an experimental test bench representative of mission scenarios. Following a detailed system identification and disturbance/uncertainty quantification part, two low-order controllers are synthesized within the structured $\mu/\mathcal{H}_\infty$ framework for both LOS stabilization and accurate LOS error generation. Both of these controllers were designed to guarantee a certain level of worst-case performance in the presence of plant uncertainties. Thanks to this novel control architecture a worst case 13 dB microvibration rejection performance is formally guaranteed across a 100 Hz bandwidth.

The control framework can be generalized to any kind of observation mission under the assumption that a similar group of sensors is installed. In this way, preliminary investigation of future LOS stabilization systems can benefit from a significant speed-up. A short demonstration of this capability is provided in the last part of the article where a Space telescope with rotating solar arrays is analyzed.

References

[1] "ECSS-E-HB-32-26A Spacecraft Mechanical Loads Analysis Handbook," ESA Requirements and Standards Division, Tech. Rep., 2013.

[2] L. P. Davis and J. F. Wilson, "Hubble space telescope reaction wheel assembly vibration isolation system, Structural dynamics and control interaction of flexible structures, NASA Report N87-22702," Tech. Rep., 1986.

[3] A. J. Bronowicki, "Vibration Isolator for Large Space Telescopes," *Journal of Spacecraft and Rockets*, vol. 43, no. 1, pp. 45–53, jan 2006.

[4] G. D. Racca, R. Laureijs, L. Stagnaro, J.-C. Salvignol, J. Lorenzo Alvarez, G. Saavedra Criado, L. Gaspar Venancio, A. Short, P. Strada, T. Bönke, C. Colombo, A. Calvi, E. Maiorano, O. Piersanti, S. Prezelus, P. Rosato, J. Pinel, H. Rozemeijer, V. Lesna, P. Musi, M. Sias, A. Anselmi, V. Cazaubiel, L. Vaillon, Y. Mellier, J. Amiaux, M. Berthé, M. Sauvage, R. Azzollini, M. Cropper, S. Pottinger, K. Jahnke, A. Ealet, T. Maciaszek, F. Pasian, A. Zacchei, R. Scaramella, J. Hoar,

R. Kohley, R. Vavrek, A. Rudolph, and M. Schmidt, "The euclid mission design," *Proc.SPIE*, vol. 9904, pp. 9904 – 9904 – 23, jul 2016.

[5] R. Masterson, D. Miller, and R. Grogan, "Development of empirical and analytical reaction wheel disturbance models," in *40th Structures, Structural Dynamics, and Materials Conference and Exhibit*, 1999, p. 1204.

[6] ——, "Development and validation of reaction wheel disturbance models: empirical model," *Journal of Sound and Vibration*, vol. 249, no. 3, pp. 575–598, jan 2002.

[7] D. Addari, G. Aglietti, and M. Remedia, "Experimental and numerical investigation of coupled microvibration dynamics for satellite reaction wheels," *Journal of Sound and Vibration*, vol. 386, pp. 225–241, jan 2017.

[8] D.-K. Kim, "Micro-vibration model and parameter estimation method of a reaction wheel assembly," *Journal of Sound and Vibration*, vol. 333, no. 18, pp. 4214–4231, sep 2014.

[9] V. Preda, "Robust Microvibration Control and Worst-case Analysis for High Pointing Stability Space Missions," Ph.D. dissertation, Université de Bordeaux, 2017.

[10] V. Preda, J. Cieslak, D. Henry, S. Bennani, and A. Falcoz, "A $\mathcal{H}_\infty/\mu$ solution for microvibration mitigation in satellites: A case study," *Journal of Sound and Vibration*, vol. 399, pp. 21–44, jul 2017.

[11] ——, "Robust microvibration mitigation and pointing performance analysis for high stability spacecraft," *International Journal of Robust and Nonlinear Control*, oct 2018.

[12] D. Kamesh, R. Pandiyan, and A. Ghosal, "Modeling, design and analysis of low frequency platform for attenuating microvibration in spacecraft," *Journal of Sound and Vibration*, vol. 329, no. 17, pp. 3431–3450, aug 2010.

[13] ——, "Passive vibration isolation of reaction wheel disturbances using a low frequency flexible space platform," *Journal of Sound and Vibration*, vol. 331, no. 6, pp. 1310–1330, mar 2012.

[14] Y. Ni, Z. Ying, and Z. Chen, "Micro-vibration suppression of equipment supported on a floor incorporating magneto-rheological elastomer core," *Journal of Sound and Vibration*, vol. 330, no. 18-19, pp. 4369–4383, aug 2011.

[15] A. Preumont, M. Horodinca, I. Romanescu, B. de Marneffe, M. Avraam, A. Deraemaeker, F. Bossens, and A. Abu Hanieh, "A six-axis single-stage active vibration isolator based on Stewart platform," *Journal of Sound and Vibration*, vol. 300, no. 3-5, pp. 644–661, mar 2007.

[16] D.-O. Lee, G. Park, and J.-H. Han, "Hybrid isolation of micro vibrations induced by reaction wheels," *Journal of Sound and Vibration*, vol. 363, pp. 1–17, feb 2016.

[17] M. Li, Y. Zhang, Y. Wang, Q. Hu, and R. Qi, "The pointing and vibration isolation integrated control method for optical payload," *Journal of Sound and Vibration*, vol. 438, pp. 441–456, jan 2019.

[18] G. Neat, J. Melody, and B. Lurie, "Vibration attenuation approach for spaceborne optical interferometers," *IEEE Transactions on Control Systems Technology*, vol. 6, no. 6, pp. 689–700, 1998.

[19] F. Boquet, F. Malric-Smith, and J.-P. Lejault, "Active and passive microvibration mitigation system for earth observation and space science missions," *Advances in the Astronautical Sciences*, vol. 141, pp. 461–480, 2011.

[20] Y. Somov, S. Butyrin, V. Matrosov, G. Anshakov, Y. Antonov, V. Makarov, A. Sorokin, N. Bashkeyev, and O. Kondrat'yev, "Ultra-precision attitude control of a large low-orbital space telescope," *Control Engineering Practice*, vol. 7, no. 9, pp. 1127–1142, sep 1999.

[21] E. Canuto, "Sub-nanometric optics stabilization in view of the GAIA astrometric mission," *Control Engineering Practice*, vol. 11, no. 5, pp. 569–578, may 2003.

[22] W. V. Miroslaw Ostaszewski, "Fine steering mirror for the james webb space telescope," *Proc.SPIE*, vol. 6665, pp. 6665 – 6665 – 10, 2007.

[23] X. Sun, B. Yang, L. Zhao, and X. Sun, "Optimal design and experimental analyses of a new micro-vibration control payload-platform," *Journal of Sound and Vibration*, vol. 374, pp. 43–60, jul 2016.

[24] *ARS-14 Sensors Datasheet*, Applied Technology Associates, 2002.

[25] A. Packard and J. Doyle, "The complex structured singular value," *Automatica*, vol. 29, no. 1, pp. 71–109, 1993.

[26] P. Gahinet and P. Apkarian, "A linear matrix inequality approach to $\mathcal{H}_\infty$ control," *International Journal of Robust and Nonlinear Control*, vol. 4, no. 4, pp. 421–448, 1994.

[27] K. Zhou, J. C. Doyle, K. Glover *et al.*, *Robust and optimal control*. Prentice Hall New Jersey, 1996, vol. 40.

[28] P. Apkarian, "Nonsmooth μ-synthesis," *International Journal of Robust and Nonlinear Control*, vol. 21, no. 13, pp. 1493–1508, 2011.

[29] P. Apkarian, M. N. Dao, and D. Noll, "Parametric robust structured control design," *IEEE Transactions on Automatic Control*, vol. 60, no. 7, pp. 1857–1869, July 2015.

[30] D. Korsch, "Anastigmatic three-mirror telescope," *Appl. Opt.*, vol. 16, no. 8, pp. 2074–2077, Aug 1977.

[31] *CONEX-LDS User's Manual*, Newport, 2017.

[32] *PZ 149E User Manual S-330 Tip/Tilt Platform*, Physik Instrumente, 2007.

[33] K. Zhou and J. Doyle, *Essentials of robust control*. Prentice Hall, 1999.

[34] L. Ljung, *System identification: theory for the user*. Prentice-hall, 1987.

[35] R. Pintelon and J. Schoukens, *Nonparametric Techniques in System Identification*. London: Springer London, 2014, pp. 1–15.

[36] P. Welch, "The use of fast fourier transform for the estimation of power spectra: a method based on time averaging over short, modified periodograms," *IEEE Transactions on audio and electroacoustics*, vol. 15, no. 2, pp. 70–73, 1967.

[37] A. Oppenheim and R. Schaffer, *Digital Signal Processing*. Prentice-hall, 1975.

[38] S. Boyd and L. Vandenberghe, *Convex Optimization*. Cambridge University Press, 2004.

[39] H. Garnier, M. Mensler, and A. Richard, "Continuous-time model identification from sampled data: Implementation issues and performance evaluation," *International Journal of Control*, vol. 76, no. 13, pp. 1337–1357, 2003.

[40] L. Ljung, "Experiments with identification of continuous time models," in *Proceedings of the 15th IFAC Symposium on System Identification*, 2009.

[41] Z.-Q. Wang, P. LUNDSTRÖM, and S. SKOGESTAD, "Representation of uncertain time delays in the $\mathcal{H}_\infty$ framework," *International Journal of Control*, vol. 59, no. 3, pp. 627–638, 1994.

[42] J. Doyle, A. Packard, and K. Zhou, "Review of lfts, lmis, and mu," in *Proceedings of the 30th IEEE Conference on Decision and Control*, 1991, pp. 1227–1232 vol.2.

[43] M. Safonov and R. Chiang, "Model reduction for robust control: A schur relative error method," *International Journal of Adaptive Control and Signal Processing*, vol. 2, no. 4, pp. 259–272, 1988.

[44] K. Zhou, "Frequency weighted model reduction with $\mathcal{L}_\infty$ error bounds," in *American Control Conference, 1993*. IEEE, 1993, pp. 2123–2127.

[45] G. Balas, R. Chiang, A. Packard, and M. Safonov, *Robust Control Toolbox User's Guide*, 2016.

[46] D. Alazard and C. Cumer, "Satellite dynamics toolbox," url: https://personnel.isae-supaero.fr/daniel-alazard/matlab-packages/satellite-dynamics-toolbox.html (Accessed: 2018-11-23), 2014.

Francesco Sanfedino received a double degree in aerospace engineering from Politecnico di Torino, Turin, Italy, and Institut Supérieur de l'Aéronautique et de l'Espace, Toulouse, France, in 2015. He received a Research Master in automatic control and signal/images treatment with the Ecole Normale Supérieure de Cachan, France, in 2015. He received a Ph.D. degree in control of microvibrations with the Institut Supérieur de l'Aéronautique et de l'Espace, the European Space Agency and Airbus Defence and Space in a Networking/Partnering Initiative. He is currently associate professor at ISAE/SUPAERO in Control of Space Systems. His current research interests include multi-body dynamics, robust control of microvibrations, design of line-of-sigth stabilization systems.

Valentin Preda obtained a master's degree from Politehnica University of Bucharest in advanced control and real-time systems and a Ph.D from University of Bordeaux on the topic of robust microvibration control in partnership with the European Space Agency (ESA) and Airbus Defence and Space, within the framework of ESA's Networking/Partnering Initiative program. He is currently working as a research fellow within the AOCS & Pointing Systems Division at ESA/ESTEC in Noordwijk, Netherlands. His main research areas include robust control, flexible and multi-body dynamics, high-bandwidth microvibration isolation and line-of-sight stabilization systems.

Valérie Pommier-Budinger received an engineering degree from Ecole Nationale des Arts et Métiers, attended the Ecole Normale Superieure de Cachan to get the Agregation (French teaching Diploma) and got a Ph.D. degree from the University of Bordeaux. She is currently Professor of System Dynamics and Control at ISAE-SUPAERO in Toulouse, France. Her research interests include design and control of active vibration control systems.

Daniel Alazard graduated from the Ecole Nationale Supérieure des Arts et Métiers (gold medal) in 1986 and received a Master in Advanced Automatic Control and Systems from SUPAERO (Ecole Nationale Supérieure de l'Aéronautique et de l'Espace) in 1987. Between 1989 and 2000 he is a research scientist at ONERA (The French Aerospace Lab). Since 2000, he is full Professor at ISAE/SUPAERO. His main research interests concern robust control, flexible structure control and their applications to various aerospace systems. He passed the Accreditation to Supervise Research in 2003 and is an AIAA associate fellow.

Fabrice Boquet graduated from ISAE (Institut Supérieur de l'Aéronautique et de l'Espace) in 1987. Between 1989 and 2014, he worked in the Space industry at Airbus Defense and Space as operations, software, AOCS and flight dynamic engineer, and as microvibration expert. Since 2014, he is working at ESA/ESTEC in Noordwijk Nederlands as Control System Engineer in the AOCS and Pointing section, and is involved in different Earth Observation and Science missions, and in several R&Ds related to high accuracy pointing, microvibration mitigation and line of sight control.

Samir Bennani obtained an M.Sc. and a Ph.D from the Technical University Delft in Aerospace Engineering with specialisation in the field of systems theory and robust control applied to flight control systems. He is currently Heading the Guidance Navigation & Control System Section at the European Space Agency (ESA), ESTEC. He contributes with his team to the preparation of many future ESA active control technologies and missions. He is a senior member of various international professional associations including the AIAA, IFAC and IEEE control systems society.